

**M A S A R Y K O V A  
U N I V E R Z I T A**

PŘÍRODOVĚDECKÁ FAKULTA

# **X-ray spectroscopy of the cosmic web**

Bakalářská práce

**MARTIN KOLÁŘ**

Vedoucí práce: prof. Mgr. Norbert Werner, Ph.D.

Ústav teoretické fyziky a astrofyziky

Brno, jaro 2024



**MUNI**  
**SCI**



## Bibliografický záznam

**Autor:** Martin Kolář  
Přírodovědecká fakulta  
Masarykova univerzita  
Ústav teoretické fyziky a astrofyziky

**Název práce:** Rentgenová spektroskopie kosmické pavučiny

**Studijní program:** Fyzika

**Obor:** Astrofyzika

**Vedoucí práce:** prof. Mgr. Norbert Werner, Ph.D.

**Akademický rok:** 2023/2024

**Počet stran:** xiv + 85

**Klíčová slova:** Rentgenová spektroskopie, Kosmická pavučina, IllustrisTNG, Chandra X-ray Observatory, XRISM, NewAthena, HUBS, LEM, SOXS, pyXSIM, Xspec



## Bibliographic Entry

**Author:** Martin Kolář  
Faculty of Science  
Masaryk University  
Department of theoretical physics and astrophysics

**Title of Thesis:** X-ray spectroscopy of the cosmic web

**Degree Programme:** Physics

**Field of Study:** Astrophysics

**Supervisor:** prof. Mgr. Norbert Werner, Ph.D.

**Academic Year:** 2023/2024

**Number of Pages:** xiv + 85

**Keywords:** X-ray spectroscopy, Cosmic web, Warm-hot intergalactic medium, IllustrisTNG, Chandra X-ray Observatory, XRISM, NewAthena, HUBS, LEM, SOXS, pyXSIM, Xspec





## **Abstrakt**

V této bakalářské práci se věnujeme simulování pozorování horkého meziga-laktického plynu v okolí masivní kupy galaxií. Tato pozorování provádíme s rentgenovými satelity současnosti i budoucnosti, tedy s Chandra ACIS-S, XRISM Resolve, NewAthena X-IFU, HUBS a LEM IFU. Ukazujeme, že schopnosti nových misí budou skutečně přesahovat schopnosti těch současných. Se satelity HUBS a LEM jsme dokázali odpozorovat přímou detekci regionu s podmínkami blízkými WHIM se signifikancí  $1\sigma$ .

## **Abstract**

In this thesis, we simulate mock observations of hot gas around a massive galaxy cluster with the X-ray instruments of today and the future, such as Chandra ACIS-S, XRISM Resolve, NewAthena X-IFU, HUBS and LEM IFU. We demonstrate, that the new satellites will indeed have capabilities exceeding the ones of the current missions. With the HUBS and LEM satellites, we report a direct detection of a WHIM-like region with  $1\sigma$  significance.

ZADÁNÍ  
BAKALÁŘSKÉ PRÁCE

Akademický rok: 2023/2024

---

**Ústav:** Ústav teoretické fyziky a astrofyziky

---

**Student:** Martin Kolář

---

**Program:** Fyzika

---

**Specializace:** Astrofyzika

---

Ředitel ústavu PŘF MU Vám ve smyslu Studijního a zkušebního řádu MU určuje bakalářskou práci s názvem:

---

**Název práce:** Rentgenová spektroskopie kosmické pavučiny

---

**Název práce anglicky:** X-ray spectroscopy of the cosmic web

---

**Jazyk závěrečné práce:** angličtina

---

**Oficiální zadání:**

Most of the ordinary baryonic matter in the low-redshift Universe resides in a low-density gaseous warm-hot intergalactic medium (WHIM) permeating the filamentary cosmic web. Surveying the distribution and the properties of the WHIM remains one of the major outstanding challenges of observational astrophysics. The student will determine the predicted properties of the WHIM in numerical cosmological simulations and simulate X-ray spectra of the WHIM for different future X-ray space observatories, with different photon collecting, imaging, and spectroscopic capabilities. These predictions will inform us about the capabilities of the different proposed and approved future missions in surveying the elusive "missing" baryonic component of the Universe.

---

**Vedoucí práce:** prof. Mgr. Norbert Werner, Ph.D.

---

**Konzultant:** Mgr. Tomáš Plšek

---

**Datum zadání práce:** 13. 11. 2023

---

**V Brně dne:** 2. 2. 2024

---

Zadání bylo schváleno prostřednictvím IS MU.

Martin Kolář, 13. 11. 2023

prof. Mgr. Norbert Werner, Ph.D., 13. 11. 2023

RNDr. Luboš Poláček, 5. 12. 2023



## Poděkování

Na tomto místě bych chtěl poděkovat všem těm, kteří stáli nejen za tím, že má tato práce hlavu a patu, ale i těm, bez nichž by celé moje studium bylo jen *marnost a honba za větrem*. Především děkuji svému vedoucímu, prof. Norbertu Wernerovi za veškerý jeho drahocenný čas, který mně a této práci věnoval. Děkuji, že mi svěřil krásné téma, že mě jím provedl a neztratil během této činnosti víru v bakalářské studentstvo. Veliký dík patří také mému konzultantu, Mgr. Tomáši Plškovi, který se mnou měl neskutečnou trpělivost, provedl mě divy praktické astronomie a zákoutími rentgenových spekter a daroval mi obdivuhodný kus svého volného času.

Děkuji svým nejbližším. Své rodině za neustálou podporu a neobyčejné zázemí, kterého si obzvláště cením. Děkuji svým přátelům a spolužákům, kteří jsou mou neustálou motivací, reflexí, oporou, neustálým vzorem i rozptýlením. Děkuji Románkovi za jeho neuvěřitelné obědy. Děkuji Adce za její přítomnost. Děkuji Lei za její houževnatost. Děkuji Pavlínce za její blízkost. Děkuji Terce za její víru. Děkuji Elišce za její odvahu. A děkuji všem ostatním, kteří se mi do odstavce nevejdou, ale v srdci je nosit nepřestávám.

I would like to express my sincere thanks to prof. Oliver Hahn for his valuable contributions during the development of this work. And, of course, I would love to thank mr. Martin Mondek, who works at Burger King.

Nakonec děkuji Bohu, že mě provází životem a že má se mnou ještě větší strpení, než můj vedoucí práce. A to je co říct.

## Prohlášení

Prohlašuji, že jsem svoji bakalářskou práci vypracoval samostatně s využitím informačních zdrojů, které jsou v práci citovány.

Martin Kolář



# Contents

|  |           |
|--|-----------|
| <b>Introduction</b>                                  | <b>1</b>  |
| <b>1 The cosmic web</b>                              | <b>3</b>  |
| 1.1 Interstellar and intergalactic gas . . . . .     | 3         |
| 1.2 X-ray spectra of hot intergalactic gas . . . . . | 5         |
| 1.2.1 Continuum . . . . .                            | 5         |
| 1.2.2 Emission lines . . . . .                       | 5         |
| 1.2.3 The study of X-ray spectra . . . . .           | 6         |
| 1.2.4 X-ray background . . . . .                     | 7         |
| 1.2.5 Obtaining X-ray spectra . . . . .              | 8         |
| 1.3 Cosmological simulations . . . . .               | 8         |
| 1.3.1 Illustris: TNG . . . . .                       | 8         |
| <b>2 X-ray spectroscopy</b>                          | <b>11</b> |
| 2.1 The evolution of X-ray spectroscopy . . . . .    | 12        |
| 2.1.1 Grating X-ray spectroscopy . . . . .           | 12        |
| 2.1.2 Microcalorimeter arrays . . . . .              | 13        |
| 2.1.3 TES microcalorimeters . . . . .                | 14        |
| 2.2 Missions focusing on X-ray astronomy . . . . .   | 15        |
| 2.2.1 Chandra X-ray Observatory . . . . .            | 16        |
| 2.2.2 XMM-Newton . . . . .                           | 17        |
| 2.2.3 ASTRO-E, Suzaku and Hitomi . . . . .           | 18        |
| 2.2.4 XRISM . . . . .                                | 19        |
| 2.2.5 Hot Universe Baryon Surveyor . . . . .         | 21        |
| 2.2.6 Athena . . . . .                               | 21        |
| 2.2.7 Line Emission Mapper . . . . .                 | 22        |
| 2.3 Main topics of modern X-ray astronomy . . . . .  | 23        |
| 2.3.1 The search of the missing baryons . . . . .    | 23        |
| 2.3.2 Accretion shocks and AGN heating . . . . .     | 25        |
| 2.3.3 Dynamics of cosmic plasma . . . . .            | 25        |
| 2.3.4 Chemical composition of the universe . . . . . | 25        |
| 2.3.5 Stars and supernova remnants . . . . .         | 26        |
| <b>3 Simulating the X-ray spectra</b>                | <b>27</b> |
| 3.1 Used packages . . . . .                          | 27        |
| 3.1.1 pyXSIM . . . . .                               | 27        |
| 3.1.2 SOXS . . . . .                                 | 27        |
| 3.1.3 Xspec . . . . .                                | 28        |
| 3.2 Handling the simulation data . . . . .           | 28        |

|          |   |           |
|----------|---|-----------|
| 3.3      | Instrument simulations . . . . .                        | 30        |
| 3.3.1    | X-ray satellites: response files . . . . .              | 30        |
| 3.3.2    | Adding custom instruments . . . . .                     | 34        |
| 3.3.3    | Simulating background radiation . . . . .               | 35        |
| 3.3.4    | Configuration of observations . . . . .                 | 36        |
| 3.3.5    | Mock observations and spectra . . . . .                 | 37        |
| 3.4      | Spectral fitting with <i>Xspec</i> . . . . .            | 38        |
| 3.4.1    | Data analysis . . . . .                                 | 39        |
| <b>4</b> | <b>Results</b>  | <b>41</b> |
| 4.1      | Halo center . . . . .                                   | 41        |
| 4.2      | Halo $r_{500}$ . . . . .                                | 42        |
| 4.3      | Halo $r_{200}$ . . . . .                                | 42        |
| 4.4      | Halo beyond $r_{200}$ . . . . .                         | 43        |
| 4.5      | WHIM filament . . . . .                                 | 43        |
| 4.6      | Data availability . . . . .                             | 44        |
| <b>5</b> | <b>Conclusion</b>                                       | <b>55</b> |
|          | <b>Bibliography</b>                                     | <b>57</b> |
| <b>A</b> | <b>Results: tables for remaining regions</b>            | <b>63</b> |
| <b>B</b> | <b>Results: all remaining fitted spectra</b>            | <b>67</b> |
| <b>C</b> | <b>Code: loading and handling of TNG data structure</b> | <b>77</b> |
| <b>D</b> | <b>Code: mock observations and spectra acquisition</b>  | <b>83</b> |



## Introduction

The everyday human experience with the universe resides undoubtedly in their immediate surroundings. We are used to the baryonic world, we were born into. Our senses made us many times so naive, we thought this might just be all the universe has to offer. It is not so long ago when humanity put the Earth away from the center of the universe. It is roughly a hundred years since we learned, that the distances to galaxies far away are far from imaginable. In the era of today, in search for new mysteries and discoveries, astrophysicists are picturing an ultimately different universe. One full of matter and energy, we are not used to. One, that is far beyond our everyday experience. In this world, baryons, the 'ordinary, everyday' matter, are in a vast shortage, making only up to a few ( $\sim 5$ ) percent of the universe. And still, in comparison to actual observations, there is a lot of it hidden somewhere beyond our grasp. Might it be in the filaments of the cosmic web as the models predict? With new missions focusing on the search, we will probably find out soon!



# 1 The cosmic web

According to the well recognised  $\Lambda$ CDM model (Schneider [30], 2015) and cosmological simulations based on it, the early universe was disturbed from its perfect homogeneity, leaving some space for the gravitational forces to tear it into quasi-independent large-scale gravitationally bound structures. Today, we refer to the set of such structures as the *cosmic web*. In current universe, it is characterised by dense regions where galaxies, galaxy groups and clusters were formed. These are connected by vast filamentary structures spanning tens of megaparsecs.

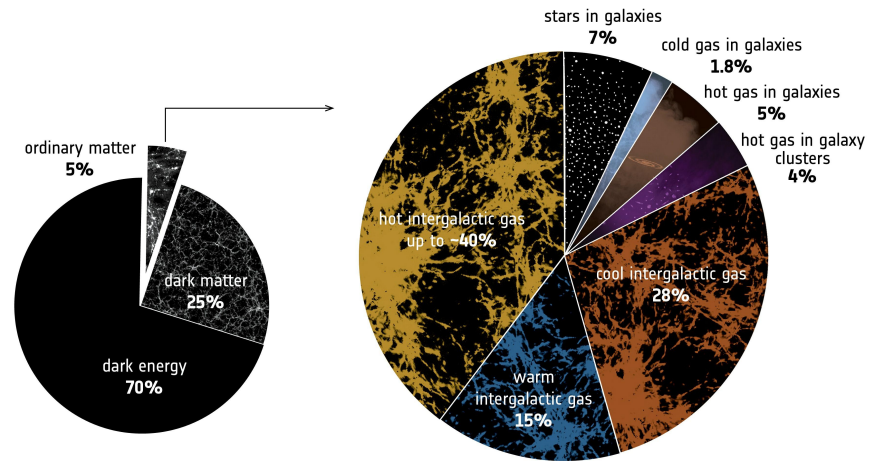


**Figure 1.1:** The distribution of energy and matter in the universe based on current observations and simulations (Nicastro [28], 2018). Note, that more than 50 % of all the ‘ordinary’ baryonic matter is in the warm-to-hot phase, being hidden in the filaments of cosmic web. Credit: *European Space Agency Science Portal* [13]

## 1.1 Interstellar and intergalactic gas

These diffuse baryons are often referred to as hot ‘atmospheric’ gas, even though it is an optically thin plasma. There are likely no major differences in the composition of such gas but we can further divide this medium simply according to where it resides. We call the hot gas close to stars and

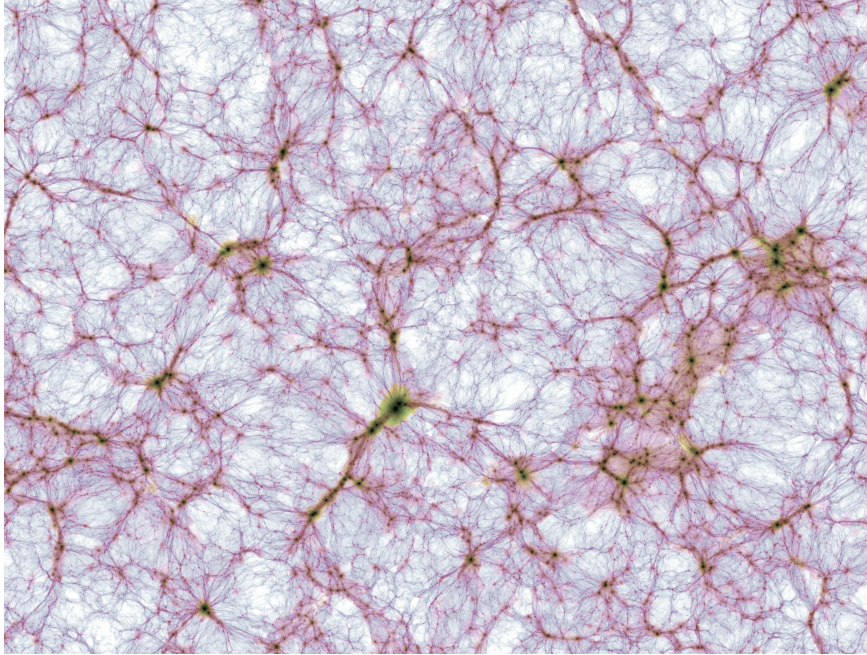


**Figure 1.2:** The baryonic gas density (brightness) and temperature (color) map of the large-scale universe as projected by Illustris TNG300 cosmological simulation. The projected region is about 370 Mpc wide in diameter horizontally. Credit: *The TNG Project* [38]

galactic cores the *interstellar medium* (ISM); further away, it is referred to as *circumgalactic medium* (CGM). If we seek larger structures, we find the *intragroup medium* (IGrM) between galaxies in galaxy groups and the *intracluster medium* (ICM) in galaxy clusters. The most hidden parts of the cosmic web and the filamentary structures further away from galaxies are called *intergalactic medium* (IGM) with its warm-to-hot phase often denoted *warm-hot intergalactic medium* (WHIM).

Due to shock heating Molnar [24], 2009, all of the WHIM, forming structures of the cosmic web, is heated to temperatures of about  $10^5$ – $10^8$  K (Cen; Ostriker [9], 1999), prohibiting star formation.

Because the properties of the intergalactic plasma are out of reach for our terrestrial laboratories, it is impossible to study it experimentally. In this section, we will try to summarise most of the theoretical knowledge regarding the WHIM and what we are expecting to observe with future missions.

Hot atmospheres - ISM/ICM/IGrM and the densest phase of the IGM - are assumed to be in *collisional ionisation equilibrium* (CIE), a state where collisions are the dominant process of excitation and ionisation among ions. It also means that the ionisation and recombination rates are equal. In less dense regions, far beyond the outskirts of massive halos, CIE is not enough to describe the gas state (Štofanová [35], 2022), but it is sufficient regarding all the regions concerned within this thesis. The following sections will introduce the main processes creating features in the spectra of ICM and WHIM. A more detailed review of this topic can be found in Werner; Mernier [41], 2020 and Kaastra [17], 2008.

## 1.2 X-ray spectra of hot intergalactic gas

All images of parts of the WHIM taken by X-ray satellites are themselves a scientific wonder, helping us map the cosmic web itself. But 2D images are only useful to some point. From the X-ray spectra, much more information can be derived, e.g. its temperature, state, composition and, if working with high-resolution spectra, even velocity dispersion.

As it is common in the field of X-ray astronomy, the wavelengths (frequencies) are represented in units of energy, in electronvolts. The X-ray scale, ranging from about 0.1 keV to over 100 keV is then divided into the soft part and the hard part of X-ray spectrum, the point of division around 10 keV. In this thesis, our focus will mostly be on the softer part of the X-ray band up to the abilities of missions conducting high-resolution X-ray spectroscopy (to around 12 keV).

### 1.2.1 Continuum

Continuum is a wide-band spectral feature created by a process occurring at a range of wavelengths. In this case, inside CIE-modelled hot cosmic plasma, electrons are free to move around, interacting with ions and being deflected from their original trajectory by electrostatic interactions. During this free-free radiation process, the energy lost is radiated away by an X-ray photon. This process is often referred to as *bremsstrahlung*. Two-photon emission or other continuum-creating processes such as Compton scattering or magnetic interactions are far less important in hot (over about  $10^{7.5}$  K) cosmic plasma.

### 1.2.2 Emission lines

When an ion directly ‘collides’ with a free electron, it may either capture it or use part of its energy to excite its own bound electron into a higher state.

The following process of de-excitation, when the bound electron releases an exact amount of energy and returns to its (mostly) original state, is known to create a photon of the same energy. When measured, this energy can tell us what specific ion was the source of this emission and into what state was its bound electron excited. These photons create narrow emission lines, and because the gas forming the diffuse baryonic component is mostly optically thin, all photons are radiated away.

Because the cosmic gas is always enriched with heavier elements, the equivalent widths of X-ray spectral lines allow us to determine the abundances of supernova products, such as O, Ne, Mg, Si, S, Ar, Ca, Fe, and Ni. Figure 1.3 shows the emission lines of different elements to be considered throughout the soft X-ray band. The study of ICM and WHIM metallicity is one of the main topics of modern X-ray astronomy and might point to the different processes of cosmic gas enrichment.

The gas temperature and density are the main parameters that determine the shape of the resulting spectrum. Whether it will be dominated by emission lines (such as in the case of low mass systems with lower temperatures) or by continuum emission.

### 1.2.3 The study of X-ray spectra

As was mentioned above, it is the X-ray spectroscopy that makes the current hunt for WHIM properties so exciting and what drives our knowledge of cosmic plasma. It is not the goal of this thesis to study the exact physical quantities from spectral fits of real observations, but having a notion of what physicists are looking for in the data is a very important link when simulating X-ray spectra for future missions.

Since we are focusing on the WHIM, the obtained quantities tell us about the state of baryons permeating the large-scale structure of the Universe. The determined properties of the plasma are its temperature, density, pressure, entropy and chemical composition.

How to look for the chemical composition of the WHIM has been already stated in the previous section 1.2.2. By measuring the equivalent width of each emission line and comparing it to other element's lines, the corresponding abundances can be found.

The bremsstrahlung continuum changes its shape according to the temperature of the observed gas, therefore the temperature can be determined from it.

The gas density can be well estimated from electron density of observed gas, which can be calculated from the overall X-ray luminosity. From all the

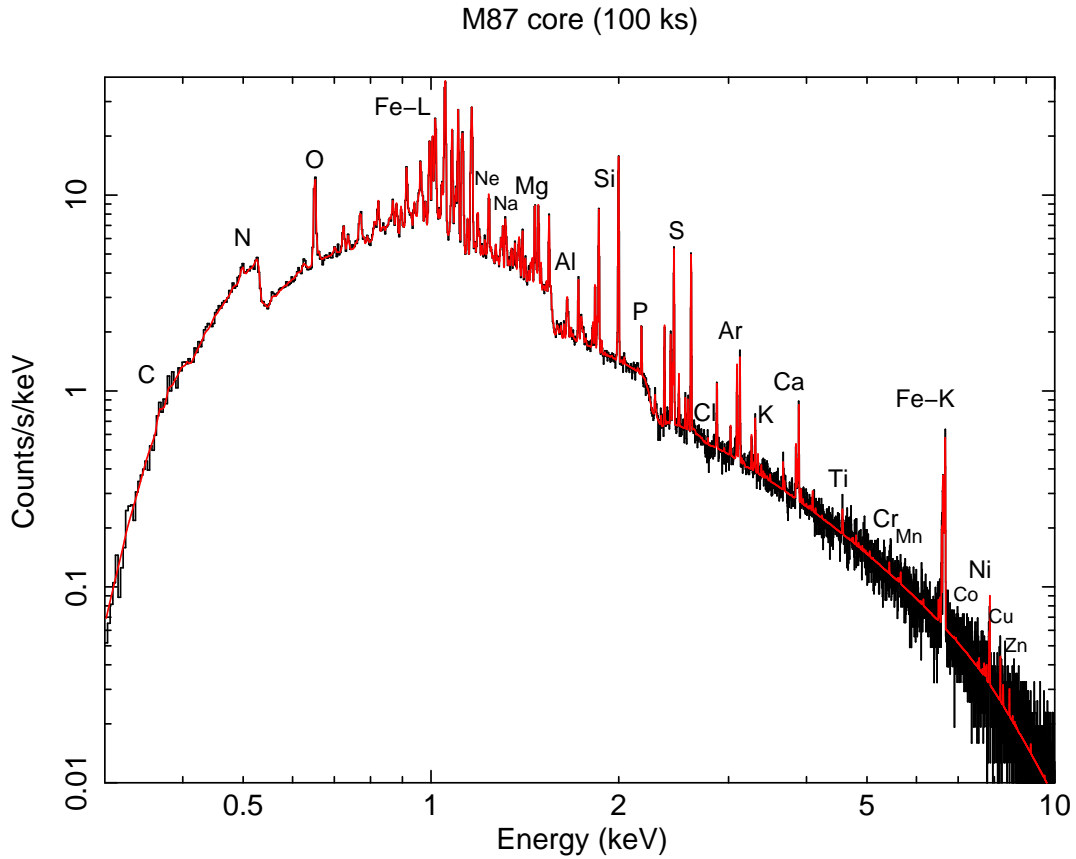


**Figure 1.3:** A simulated X-ray spectrum of the center of M87 galaxy, observed by Hitomi with a 100 ks exposition time. Fit (in red) reveals a large number of emission lines of highly ionised elements. Since the observed region is very hot, the spectrum is shaped by a great amount of bremsstrahlung continuum radiation. Credit: Kitayama [18], 2014

quantities mentioned above, all the remaining thermodynamic properties can be derived – such as entropy and pressure, as mentioned above.

#### 1.2.4 X-ray background

The obtained spectra are not always as legible as expected by ideal model observations. The Sun is partly contributing to the overall X-ray noise and also, when observing extragalactic sources, our Galaxy is a source of several X-ray emission lines, which have to be well identified and isolated in obtained spectra for proper analysis (Kraft [20], 2022).

When observing very faint sources, such as the WHIM, background radiation can be a critical component in determining the significance of all measured quantities. The instrumental background of X-ray calorimeter detectors is often very low and negligible in comparison to the X-ray background radiation caused by the local hot bubble and the hot Galactic halo. This creates another challenge when designing an X-ray mission and puts constraints on how precisely can we measure almost any of the hot gas properties mentioned above.

### 1.2.5 Obtaining X-ray spectra

Actual observations of intercluster filaments are rare. It is complicated to build and operate observatories probing regions with such faint emission. So far, the most successful attempts to map the WHIM were done either by observing distant active galactic nuclei (AGN) (probing small parts of the WHIM filaments interacting with AGN radiation in absorption: Kovács [19], 2019) or by direct observations close to massive galaxy clusters or groups, where the emissivity of hot gas is relatively high (Werner [43], 2008).<sup>1</sup>

Due to all the technical requirements for X-ray imaging and spectroscopy, this field of observational astronomy is still in its ‘early days’. More missions dedicated to the study and mapping of WHIM in X-rays are yet to be launched with great expectations and even greater visions.

## 1.3 Cosmological simulations

The creation of cosmological simulations based on popular models of the universe are a natural response to our inability to effectively observe the large-scale structure of the universe, along with its evolution. By comparing simulations to observations, we might be able to confirm or refuse multiple cosmological models, leading to a better understanding of the universe we live in.

### 1.3.1 Illustris: TNG

Various simulations are run today, some very complex, some more simple. Among them, the recent release of IllustrisTNG project results is peaking in complexity, offering a multiple-scale, multiple-resolution  $\Lambda$ CDM probe into the evolution of the universe from multiple viewpoints, thus being useful for

---

1. The X-ray emissivity scales with hot gas density to the power of two such as  $\epsilon \propto n_{\text{gas}}^2$  (Werner; Mernier [41], 2020).



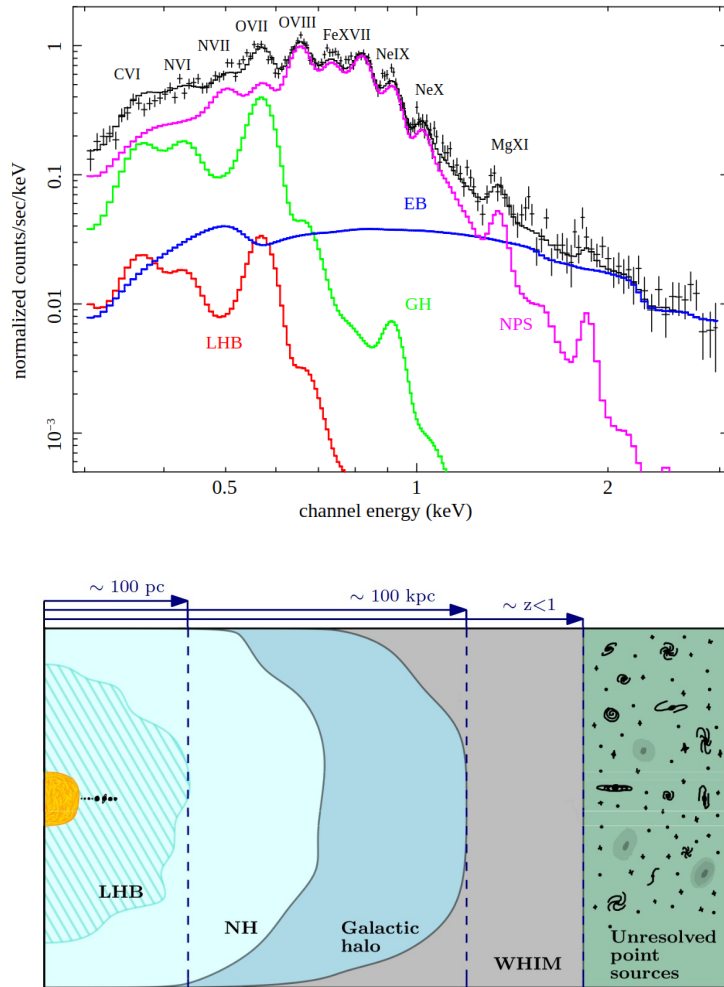


**Figure 1.4:** The X-ray background radiation components. Observations across the X-ray spectrum are burdened by local sources similarly to optical terrestrial observations, corrupted by the Earth's atmosphere. The sources include the *Local Hot Bubble* and *Galactic Halo* in the soft X-ray band. The hard band background is dominated by the *Extragalactic Background* (unresolved point sources). The region abbreviated as NPS is the north polar spur hot gas emission, as observed directly by Suzaku XIS. Usually, the NPS emission is not dominant in the spectrum. Adapted from: Miller [23], 2008 and Svačinková [36], 2023

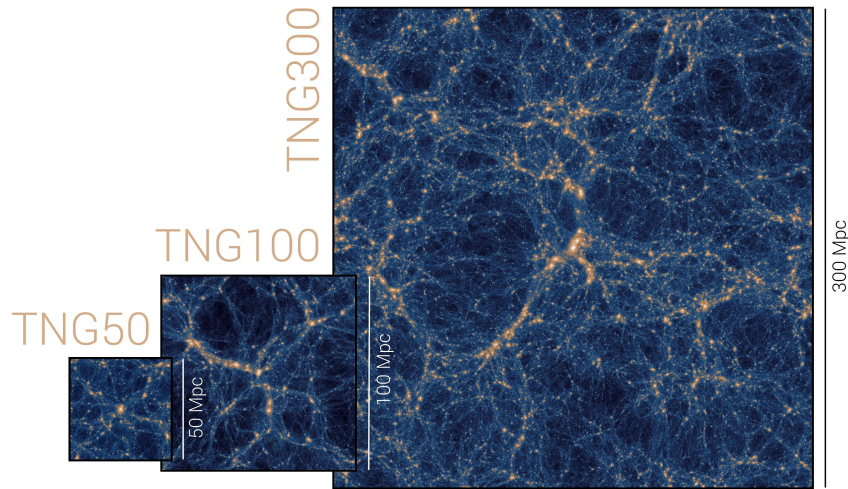


**Figure 1.5:** An illustration of the three available volumes of TNG simulations, mapping dark matter density. Credit: *The TNG Project* [38]

almost any cosmological simulation related research. TNG gravomagneto-hydrodynamical simulations consist (so far) in total of 18 simulations across three volumes. TNG50, TNG100 and TNG300 are the available sizes representing roughly 50, 100 and 300  $\text{Mpc}^3$  boxes. TNG simulations come in three resolutions. All TNG runs are modelling the evolution of dark and baryonic matter, star formation and supermassive black hole activity (Zingler [47], 2020) within 100 snapshots representing universe at different redshifts (Nelson [27], 2019). The new (so far not publicly available) TNG-Cluster simulation offers a smaller-scale large cluster-only snapshot with increased resolution (Nelson [26], 2024).

## 2 X-ray spectroscopy

It is not a simple task to conduct astronomical observations in the X-ray band. The technology needed for even the simplest of observations is demanding and complex and comes hand in hand with added challenges. For starters, it is impossible to observe the X-ray universe directly from Earth's surface. This is why all of the collected data we have today rely on space based satellite observations. The detection of X-ray photons is also more of a treasure hunt than comfortable research. X-ray flux of the most X-ray luminous object in the night sky – the Crab Nebula – is about  $4 \text{ photons cm}^{-2} \text{ s}^{-1}$ , so for successful observations, long exposure times and large photon collecting areas are demanded.

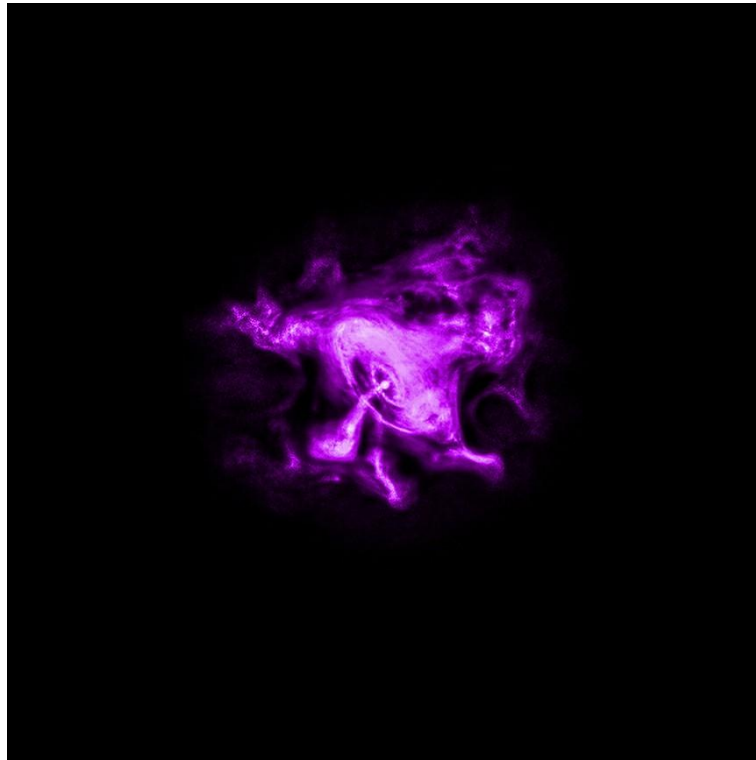


**Figure 2.1:** The Crab Nebula as observed by Chandra in X-rays. Credit: *Chandra X-ray Observatory* [10]

All spectroscopic measurements are further burdened by finite spectral resolution  $\Delta E$ , which is a function of energy itself and which limits the information given by an obtained spectrum and depends massively on the technology used for photon detection. For statistical purposes, we can also

define resolving power  $R = E/\Delta E = \lambda/\Delta\lambda$ . These technical details will be referred to in the following chapters.

### 2.1 The evolution of X-ray spectroscopy

The first successful attempts to measure X-ray radiation with satellite missions were done by proportional counters, tubes filled with gas, capturing photons and transferring their energy into signal. The first mission to implement such devices was the Uhuru satellite, and many followed. Because of the limitations of this technology, the Einstein observatory, launched later, used Solid State spectrometers – like the Bragg Crystal Spectrometer – limited only by the inability to obtain spectra in all possible wavelengths simultaneously.

The next step towards high-resolution spectroscopy in X-rays were diffraction (reflection) gratings, used until this day onboard Chandra X-ray Observatory and XMM-Newton. Dispersion spectroscopy is a very useful tool regarding the study of point sources, but its use is very limited in terms of extended sources.

The next generation of X-ray spectroscopy is being slowly but steadily revealed. Microcalorimetry can yield high-resolution spectra with comparable or better resolution than that of CCD grating spectroscopy. With the few results of Hitomi and XRISM satellites, we know how powerful this ‘new’ tool can be, and on the horizon, Transition-Edge Spectrometer microcalorimeters will soon be making their way into orbit.

#### 2.1.1 Grating X-ray spectroscopy

Diffraction and reflection grating X-ray spectroscopy takes advantage of the refraction and reflection of light. All detected photons are focused into sensitive spectrometers, their path depending on their respective energy (wavelength) and as a cone of light, this spectrum is then spread across a set of CCD detectors, converting photon energy to electrons and performing the measurement.

A disadvantage of such an approach is the inability to effectively observe extended sources, as was mentioned above, due to a dispersion effect caused by the spectrometer design. A challenge is therefore only to distinguish the dispersion effect from the correctly reflected photon paths, but for WHIM observations, even a careful approach to data analysis would bear no results. But gratings are still very useful tools regarding point sources in soft X-ray band, with Chandra reaching resolving power  $R \sim 10^3$  at around 1 keV, which is for example a goal of the HUBS satellite with a far more ad-

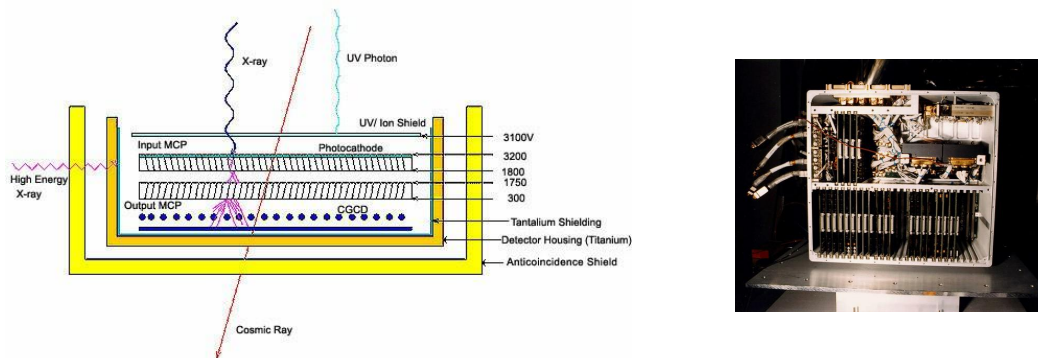


**Figure 2.2:** HRC – the High Resolution Camera grating spectrometer onboard Chandra X-Ray Observatory. A simplified scheme and picture of the actual payload before launch in 1999. Credit: Bambi; Jiang [6], 2023

vanced technology<sup>1</sup>. New designs of grating X-ray spectrometers are being developed, so it seems that in soft X-rays, it still hasn't said its last word yet.

### 2.1.2 Microcalorimeter arrays

In 1999, a short sounding rocket experiment was performed, surveying the night sky in X-rays using a microcalorimeter for the very first time in history (McCammon [22], 2002). This yielded spectra over the soft X-ray band (up to 1 keV) with an excellent energy resolution of 5–12 eV. Very similar microcalorimeters were used by JAXA on Hitomi satellite and are now being used on XRISM.

Microcalorimeter detectors use arrays of sensitive small-thermal-capacity-calorimeters, measuring the change of temperature when a single X-ray photon reaches the detector. The photons are focused into an absorber, causing a steep rise in temperature  $\Delta T$ . The energy of individual photons can be then found easily by<sup>2</sup>  $E = C \cdot \Delta T$ , where  $C$  is the heat capacity of used medium. After this rise, the excess temperature is transferred by a thermal link into a heat sink until a quasi-equilibrium is reached.

The advantage of this design, in comparison to gratings, is its ability to reach a relatively high resolving power even at higher energies, over 1 keV and higher. The energy resolution of microcalorimeters is (directly) proportional only to the absorber temperature, therefore remains constant across

1. Of course, the missions of the future are expected to exceed those of today. The ultimately different design of HUBS will make it far more efficient than Chandra with increasing photon energy (Cui [12], 2020).

2. This relation is only an illustrative simplification of the whole process.

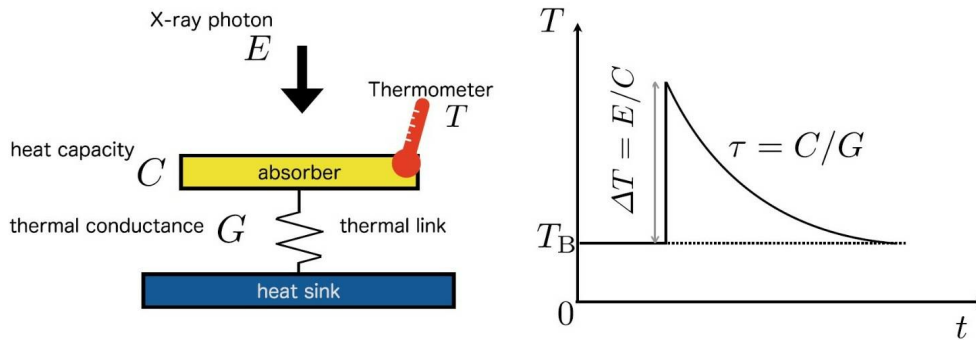


**Figure 2.3:** A simple scheme of how ordinary X-ray photon microcalorimeters work. Credit: Bambi; Jiang [6], 2023

the whole energy spectrum. Because of this, all microcalorimeter absorbers are to be kept at as low temperatures as possible, reaching now about 50 mK. Because microcalorimeter arrays are non-dispersive detectors, their use is not limited to point sources only, allowing us to probe all interesting X-ray sources, potentially including the cosmic web and its properties, in more detail.

### 2.1.3 TES microcalorimeters

The Transition Edge Sensor microcalorimeter design is in many ways comparable to ordinary microcalorimeters, introduced in the previous subsection. Instead of directly measuring the temperature rise with a microcalorimeter, a superconducting material is heated. Superconductors are defined having a certain (material dependent) critical temperature  $T_C$  at the transition between the ordinary material phase and superconductivity. There even the slightest change in temperature can ‘drastically’ change its conducting capabilities, i.e. its resistance.

TESs are now designed to be kept at the temperature level given by  $T_C$  (usually around 0.1 K) so when an X-ray photon hits the TES detector, the used material becomes non-superconductive and a process is underway to reduce the temperature to stable  $T_C$  again. The change of resistance is easily measured, the excess heat is quickly transferred into a heat sink. To illustrate TES microcalorimeter detector designs, see Fig. 2.4.

The future of TES designed X-ray spectroscopic missions is yet to be written. The great success of microcalorimeters is yet to be introduced by XRISM and the TES arrays are to follow in upcoming mission designs such as Athena (NewAthena), LEM or HUBS. TESs promise to come especially

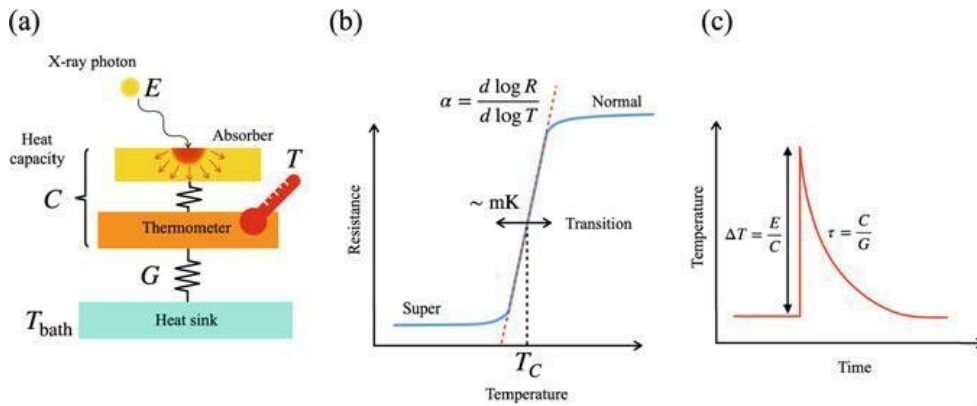


**Figure 2.4:** A simple scheme of how TES microcalorimeters detect X-ray photons. Credit: Bambi; Jiang [6], 2023

with enhanced energy resolution capabilities (possibly around only 1 eV over the whole spectrum in some cases). Its design is more complex than that of Hitomi and XRISM microcalorimeter arrays so possible trade-offs for better resolution will be a smaller collecting area or field of view. That's why most future X-ray spectroscopic missions come along with another less complicated instrument with large field of view – an imager. If nothing else, it may very well be used to create pretty images!

For a more detailed description of the topic, please see Bambi; Jiang [6], 2023 and references therein.

## 2.2 Missions focusing on X-ray astronomy

In the following section of this thesis, our focus will be on missions currently operating and on X-ray mission concepts planned to launch in the near future. However, it would have been a great shame, if there was no memorial built for all the predecessor X-ray missions of the past, for they are not to be ever forgotten.

The X-ray universe with its countless secrets has been observed for decades now, with the first steps being the *Vela* constellation or X-ray dedicated *Uhuru*. The imaging capabilities of *The Einstein Observatory* have produced the first X-ray images of the universe. The first ESA X-ray mission *EXOSAT* or Japanese missions *Hakucho* and the *ASTRO-* series of missions were further milestones in observations of X-ray transients or solar observations. At the end of the European *ROSAT* mission in 1999, we were gifted with the very first X-ray all-sky survey catalog consisting of more than 150 000 objects. Apart from satellites of our focus, the hard X-ray satellite

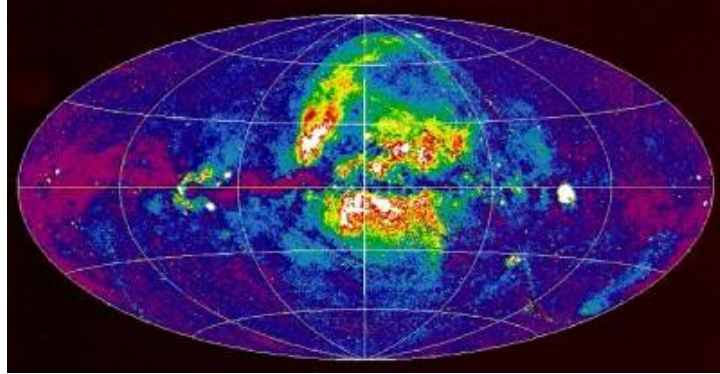


**Figure 2.5:** The ROSAT all-sky survey. Panorama of the X-ray sky from 1 to 100 keV as observed by the satellite between the years 1991–1997. Credit: *European Space Agency Science Portal* [13]

*NuSTAR* launched in 2012 and, in the hunt for a new X-ray all-sky survey, the German-Russian mission *eROSITA* was launched in 2019 as a younger successor to *ROSAT* with better resolution and larger field of view.

### 2.2.1 Chandra X-ray Observatory

Chandra, a satellite named after Subrahmanyan Chandrasekhar, the Nobel Prize laureate, is one of the four *Great Observatories* of NASA. It occupies such a place alongside the Hubble Space Telescope, Compton Gamma-Ray Observatory and Spitzer Space Telescope, which by itself underlines its scientific significance. Chandra was launched in July 1999 and, although being a bit outdated in comparison to new planned missions such as Athena or LEM, it remains a valued well of X-ray data of the universe. Being more than twenty years in orbit, Chandra is still fully operational.

Chandra's HRMA (High-Resolution Mirror Assembly) consists of two sets of mirrors coated with iridium and has angular resolution better than 0.5 arcsec. At the time of assembly, those were the smoothest mirrors ever created. X-ray photons are resolved in CCD grating spectrometers and imagers ACIS<sup>3</sup> and HRC<sup>3</sup> in X-ray band range of 0.06–10 keV with about 120–200 eV resolution across the harder part of the X-ray spectrum. At about 1 keV, ACIS's High-Energy Transmission Grating (HETG) is able to observe spectra with up to the resolution of 1 eV. In addition to beautiful images of hot X-ray sources by HRC's large field of view, Chandra has so far been an endless source of X-ray spectra and light curves (Bambi; Jiang [6], **2023**).

---

3. The Advanced CCD Imaging Spectrometer and the High-Resolution Camera.



Unfortunately, due to its relatively high hard X-ray grating resolution, it is virtually unable to resolve individual lines in its spectra beyond the soft X-ray band and is also not equipped to observe in detail the faint filamentary structures which are of interest of this thesis. Chandra has been known to observe the most luminous parts of such structures with high gas densities and temperatures as well as various point sources.

### 2.2.2 XMM-Newton

Still operating today, ESA's XMM-Newton (launched in 1999) is, along with Chandra, one of the greatest X-ray observatories at orbit. Citing from its user's handbook: *'It is (...) clear that Chandra and XMM-Newton have complementary characteristics and that both have constituted a new generation of X-ray missions, with enormously improved capabilities compared to their predecessors ASCA, ROSAT and RXTE.'*<sup>4</sup> We can think of XMM-Newton, Chandra and Suzaku as of great milestones shaping X-ray astronomy into the picture we see today.

XMM-Newton consists of three X-ray telescopes and one 30 cm optical/UV telescope. At ordinary conditions, all of these can operate at the same time, resolving the universe at multiple wavelengths, which adds to the total scientific value of obtained data. Beyond the X-ray telescopes are located two EPIC MOS detectors and one EPIC pn detector<sup>5</sup>. Together they add to a field of view of 30 arcmin, operating at 0.2–12 keV with about 75 eV resolution as for today. For calibration purposes, XMM-Newton is frequently observing the Crab Pulsar. The EPIC pn instrument is used for its fast readout and for observing rapidly variable objects with about 30  $\mu$ s time resolution in a special observation mode. To filter optical reflected light being detected on the CCD cameras, filters with various thickness are installed.

The spectrometer used onboard of XMM-Newton is called RGS, the Reflection Grating Spectrometer. Two of those are used for high resolution spectroscopy mostly at longer wavelengths. In soft X-ray band of about 0.33–2.5 keV, it can resolve spectra with a resolution of  $\sim 4$  eV. This is the region of most interest to most astronomers, where a plenty of emission lines can be found within the spectra. The optical/UV detector is named the Optical Monitor (OM) and is used for imaging of the optical light collected by XMM-Newton's telescope. It is to be used only for very faint sources with optical magnitudes higher than 7.4 mag, but is able to produce spectra in

4. *XMM-Newton Users Handbook* [44], 2023, p. 154

5. The European Photon Imaging Camera – Metal Oxide Semiconductor and *pn*.

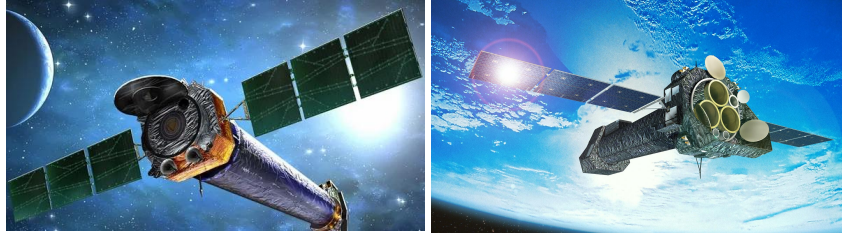


**Figure 2.6:** The two great X-ray observatories, surveying the X-ray and far UV sky until this day with CCD resolution, operating for about 25 years now. From left to right: Chandra X-ray Observatory and XMM-Newton. Credit: *NASA Science* [25] and *European Space Agency Science Portal* [13]

those wavelength ranges. Those can be later compared to the resolved X-ray spectra.

Similarly to Chandra, XMM-Newton is more than capable of observing single bright X-ray sources and has produced countless spectra during its lifetime. Even though XMM-Newton likely experienced a few micrometeorite impacts and an unhealthy saturation of OM, until this day it continues to successfully observe the X-ray/UV/optical universe.

### 2.2.3 ASTRO-E, Suzaku and Hitomi

Astro-E was the first satellite to carry an X-ray microcalorimeter on board. It launched in 2000 but was lost during a failure in launch and never conducted any measurements. In response to this unfortunate event, JAXA developed a similar machine comparable to ASTRO-E: ASTRO-E2. Soon after its launch, Suzaku, as it was named after a successful launch into orbit in 2005, experienced a helium leak from a tank supporting its cooling system. Without proper cooling, the onboard microcalorimeter was deemed useless and although Suzaku continued to measure X-ray spectra of many sources for years to come, its most valued scientific potential was ultimately lost. Even though the Suzaku mission 'failed', it remains the first to deliver an X-ray microcalorimeter to space.

Hitomi, also called Astro-H, was yet another JAXA project to resolve X-ray universe using a microcalorimeter array. In its design, it followed its predecessors, inheriting the Suzaku detector with only a bit of novelty. In hopes of obtaining revolutionary X-ray spectra, Hitomi was launched from Tanegashima in 2016 and was successfully delivered to its orbit. Most unfortunately, JAXA lost contact with Hitomi about a month later. The satellite was lost because of attitude control system failure. Before this happened,

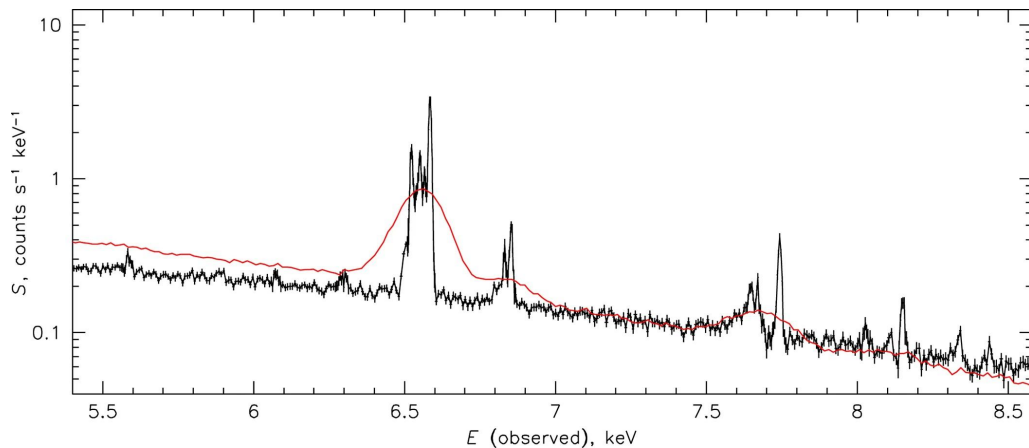


**Figure 2.7:** A quick comparison of a CCD spectrum (in red) obtained by Suzaku and a simulated microcalorimeter spectrum (in black) from the Hitomi satellite. In higher energy X-rays, the spectra obtained by microcalorimeter-based missions are superior to those with CCD resolution. Credit: Hitomi Collaboration [15], 2016

Hitomi managed to survey a part of the Perseus cluster of galaxies but due to this being a rushed event, not all calibration was yet performed. Nevertheless the obtained spectra give us a picture about how exciting it is to have data from microcalorimeter surveys.

#### 2.2.4 XRISM

In September 2023, after almost twenty-three years of unsuccessful or just partially successful attempts, JAXA managed to deliver one fully operational X-ray microcalorimeter into orbit. Onboard of XRISM, it is today revolutionising our view of the whole X-ray universe.

XRISM, a successor of Hitomi, equipped with almost identical instruments, consists of two separate detectors: Resolve and Xtend, both having the same mirror assembly (XMA) coated with aluminium.

The Xtend tool is relatable to Chandra’s HRC having a relatively large field of view ( $30 \text{ arcmin}^2$ ) and a resolution of a CCD camera. It is introduced as an soft X-ray imager and operates at a temperature of  $-120^\circ\text{C}$ . Its main purpose is to observe targets simultaneously with Resolve and produce images of larger regions.

Being undoubtedly the most valued detector onboard, Resolve consists of a microcalorimeter array of HeTe absorbers in silicon. As it stands for a microcalorimeter detector, it needs to be constantly cooled to retain temper-

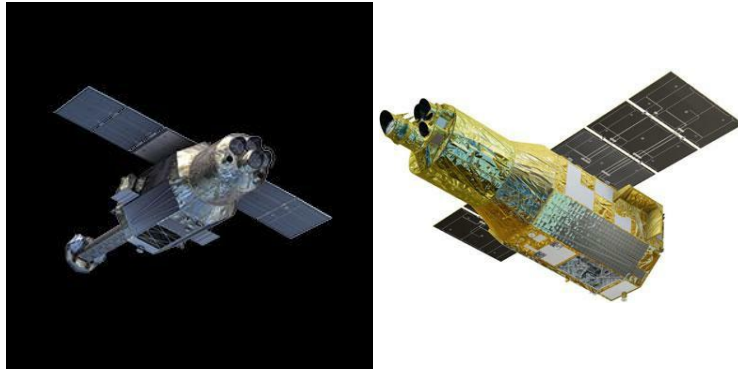


**Figure 2.8:** The Japanese X-ray satellites. From left to right: Hitomi, that was unfortunately lost in 2016 and XRISM, surveying the X-ray sky today. Credit: *High Energy Astrophysics Science Archive Research Center* [14] and Bambi; Jiang [6]

atures of around  $\sim 50$  mK which is achieved by multiple cooling procedures (see *XRISM Quick Reference* [45], 2022 for a more detailed description). With a resolution of less than 7 eV at a large spectral band of 0.3–12 keV with a small field of view, Resolve is the most scientifically important instrument onboard the satellite. Another advantage of Resolve is the absence of dispersion in creation of spectra which means, unlike XMM-Newton or Chandra, it does not lose the spatial information of its data. On top of that, Resolve is equipped with a set of five different filters including a Fe-55 calibration filter, an empty one, beryllium, polyimide-aluminium and neutral-density filter.

In their white paper (*Science with the X-ray Imaging and Spectroscopy Mission (XRISM)* [32], 2022), XRISM team promises to shed light upon vast fields of astronomy including black hole outflows, galaxy evolution, supernova remnants, evolution of stars and compact objects and larger structures such as the properties of ICM, IGM and WHIM, which are the main topics of this thesis.

Unfortunately, as for May 2024, the gate valve of XRISM has not been opened. From the practical perspective, this means that XRISM can no longer observe in the soft X-ray band (up to about 1.5 keV), since only harder X-ray photons will be detected by the Resolve instrument. Therefore, in this thesis, we will not simulate the XRISM observations under 1.5 keV.

### 2.2.5 Hot Universe Baryon Surveyor

The Hot Universe Baryon Surveyor (HUBS) mission is a Chinese proposed concept for an X-ray satellite hoping to manage to launch around the year 2030. So far a prototype has been constructed and tested in a laboratory and the design results are promising (Cui [12], 2020).

The HUBS satellite will consist of a large  $1 \text{ deg}^2$  field of view X-ray telescope of ordinary design, focusing photons onto an array of TES Mo-Cu microcalorimeters. These spectrometers will operate at extremely low temperatures with angular resolution of about 1 arcmin and are expected to produce spectra with energy resolution  $< 2 \text{ eV}$  in the soft part of X-ray band (0.2–2 keV). Due to its large grasp – the product of field of view and effective photon collecting area – HUBS can theoretically be just the mission we need for effective observations of faint intergalactic gas.

Aside from that, HUBS's focus will be on distinguishing the ICM and CGM in individual galaxies, galaxy clusters and groups. Being so far just a proposed project, HUBS satellite, its components and mission focus may be all a subject to a change in the near future.

### 2.2.6 Athena

Advanced Telescope for High ENergy Astrophysics, the Athena X-ray observatory is a 2014 selected project of ESA, currently in progress with launch expected in the 2030's. Similarly to HUBS, it aims to conduct X-ray spectroscopy using a TES microcalorimeter. The NewAthena (a redesign of the original project) will consist of a single telescope with two main instruments nested inside: the Wide-Field Imager (WFI) and the X-ray Integral Field Unit (X-IFU) (*Science with the Athena X-ray Integral Field Unit, X-IFU Preliminary Requirements Review* [31], 2019).

Of the most scientific interest remains the X-IFU, an array of TES microcalorimeters, promising to resolve spectra at a range of 0.2–12.0 keV with an energy resolution of less than 2.5 eV up to 7 keV. That will be, for example, enough to study a plenty of yet hidden emission lines in the WHIM. As it stands for a microcalorimeter, X-IFU will be constantly cooled to very low operational temperatures of about 50 mK. The other instrument, WFI, being a very fast Silicon Active Pixel Sensor camera with a large field of view, will provide further imaging in the soft X-ray band. One of the most valued scientific drives is Athena's ability to observe very distant structures, far beyond the reach of the current X-ray missions. The possibility to observe the cosmic web at redshift of  $z \approx 3$  will enable us to study not only the current composition and characteristics of the greatest structures in our universe but also their evolution in time.

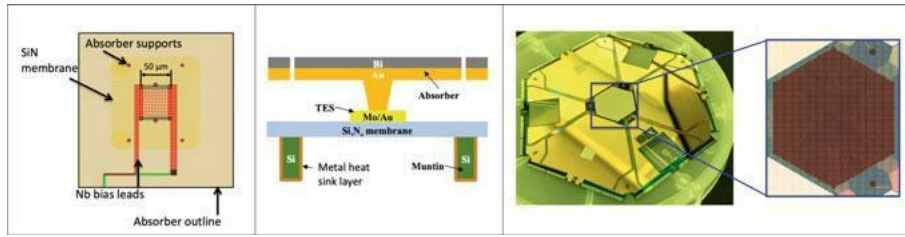


**Figure 2.9:** Athena: X-IFU instrument. From left to right: a single TES microcalorimeter pixel; the same pixel viewed as a cross-section; the Athena X-IFU prototype with the central array consisting of more than 3000 calorimeters. Credit: Bambi; Jiang [6]

The Athena team and ESA have announced that they are very open to observation proposals and want to spend the lifetime of Athena as productively as possible. The observatory has a life expectancy of five years.

### 2.2.7 Line Emission Mapper

The Line Emission Mapper (LEM) satellite concept is a mission with comparable imaging capabilities to XMM-Newton’s EPIC with better spectral resolution given by its microcalorimeter design. Or as the LEM team introduces the satellite: *it is useful to think of LEM as an XMM-Newton with a calorimeter.*<sup>6</sup> Being now just a concept, it is not yet certain if LEM will be selected to launch by NASA.

Under 1.5 m diameter mirror, an array of TES microcalorimeter detectors (similar to ATHENA and HUBS) will be nested, again operating under extreme temperature of 35–50 mK. LEM is expected to operate in soft X-rays (projected 0.2–2 keV) with a resolution reaching 1 eV across the spectrum in the middle of its field of view. It will be equipped with Integral Field Unit (IFU) non-dispersive spectrometer. To enhance its observational capabilities beyond XRISM or Athena, LEM is said to have the most effective grasp (Kraft [20], 2022).

How and where the spacecraft will be positioned is currently under study, along with talks about an all-sky soft X-ray survey and observations of the Earth.

The authors of the LEM concept praise the capabilities of their mission as it will be a great tool to study galaxy formation and feedback from newborn stars and black holes. LEM will be able to especially resolve the properties of IGM and ICM, such as its densities, temperatures, entropy, dynamics and

6. cit. from Kraft [20], 2022 [p. 12]



**Figure 2.10:** High resolution X-ray spectroscopy missions of the future. From left to right: The HUBS, NewAthena and LEM satellite concepts. Credit: *HUBS mission webpage* [16], *Athena mission webpage* [4] and Kraft [20], **2022**

overall chemical composition of mentioned gas. The great grasp of LEM is what makes it a promising tool for the study of WHIM, extended sources and its properties.

**Table 2.1:** A comparison of all the new missions instrument capabilities. Adapted from: Kraft [20], **2022**.

|  | XRISM Resolve | NewAthena X-IFU | HUBS  | LEM IFU |
|--|---------------|-----------------|-------|---------|
| Energy band [keV]                            | 0.4–12        | 0.2–12          | 0.2–2 | 0.2–2   |
| Field of view [arcmin]                       | 3             | 5               | 60    | 30      |
| Effective area at 0.5 keV [cm <sup>2</sup> ] | 50            | 6000            | 500   | 1600    |
| Angular resolution [arcsec]                  | 75            | 5               | 60    | 15      |
| Spectral resolution [eV]                     | 7             | 2.5             | 2     | 1       |

## 2.3 Main topics of modern X-ray astronomy

All proposed X-ray missions do have a certain goal they wish to accomplish, a physical phenomena to probe or explore in more detail. In most cases, this expands to more than one addressed issue from obtaining beautiful images to uncovering the greatest mysteries the universe is yet hiding beyond our reach. In the following sections, only some of the most fundamental physical problems that are being constantly probed by X-ray instruments are addressed.

### 2.3.1 The search of the missing baryons

The hot baryonic matter, of which the filamentary structures of the cosmic web are made, is so sparse we have not yet effectively observed it. The methods of observing such structures are delicate. As mentioned above, so

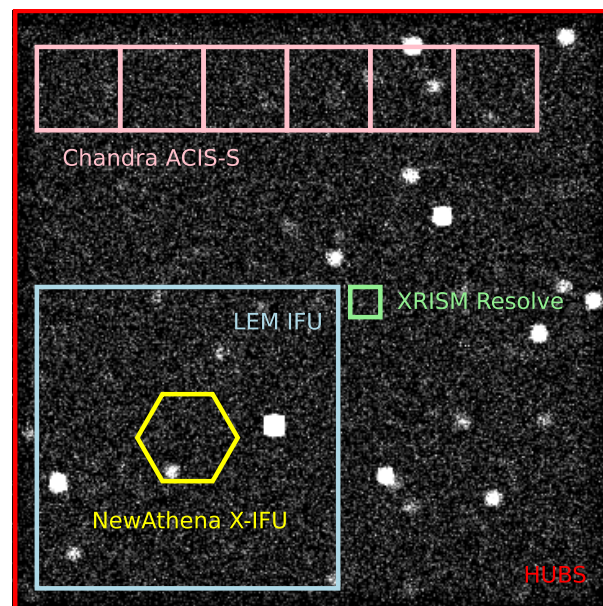


**Figure 2.11:** A comparison of the field of view of selected X-ray missions and instruments. During our simulated observations, all were centered at the same point, this figure is only an illustration.



far it has been observed only in absorption spectra when a supernova, or a similarly bright event, helped us see the invisible. With the help of TES microcalorimeter surveyors, mapping those filaments might just be a far easier task (Bregman [7], 2023).

### 2.3.2 Accretion shocks and AGN heating

One of the possible explanations of the intergalactic and intracluster gas being so hot it can not form new stars might be shock heating due to accretion shocks. This is a not yet very well understood process and to obtain the important answers, AGN feedback processes should be studied. During its active phase, compact galactic cores are known to form massive jets, driving large amounts of energy and matter from its host galaxy into outer space. These ejecta further interact with the, so far, cooling non-galactic gas, heating it to such temperatures, that we can observe it in X-rays. Observations of active compact objects as well as areas of interaction will help us further deepen our understanding of this process (Werner [42], 2019).

A similarity can be seen among much smaller radii, on the scale of star forming regions and molecular clouds. Supernovae and massive stars are driving stellar winds across their neighbourhood, heating the surrounding gas, not allowing any other stars to form in their vicinity (Bregman [7], 2023) (Kraft [20], 2022).

### 2.3.3 Dynamics of cosmic plasma

Not only thermal shock are responsible for the motion of gas in between galaxy clusters or in the filamentary structures. Multiple processes may play a vital role in directing the motion of the whole structures as well as in creating small instabilities within the local plasma. Galactic mergers and interactions, magnetic fields in the ICM, distribution of dark matter and much more may have shaped the cosmic web into the form we see today. And even now, with detailed maps of gas motions, we may get a better picture of its behavior and evolution (Bregman [7], 2023).

### 2.3.4 Chemical composition of the universe

By reading emission/absorption lines in the spectra of any observed hot X-ray visible region, one can derive the chemical composition of such regions. Multiple bright sources were observed so far but only a few fine measurements of faint cosmic web regions were conducted. With the upcoming X-ray observatories not only the chemical composition of the local universe could be stated but also the chemical composition of earlier universe to up

to  $z \approx 3$ . This can give us not only a constant abundance information but also a very valuable time dependent relation that could help to deepen our understanding of the evolution of the universe itself (Kraft [20], **2022**).

### 2.3.5 Stars and supernova remnants

A great number of stars are confirmed to be X-ray sources. It is thought that many different processes are creating this X-ray luminosity and such processes are dependent on the star type, stage of life, etc. Apart of that, cataclysmic variables and extreme events such as supernova explosions or remnants are all observable in X-ray radiation (Bambi; Jiang [6], **2023**).

Not only the deaths of stars are worth observing. As was mentioned above, their births are also a not yet fully understood mystery. With X-ray spectroscopy and observations, star forming regions or even molecular clouds forming star babies could be probed in the future (Bregman [7], **2023**).

There is much more to this topic. The list of possible observations and discoveries seems almost endless. Every proposed scientific X-ray mission consist of many ideas of what to observe, not even mentioning all the technological wonders that are created for those missions to be possible. The ideas even include observations of Solar system planet's atmospheres, probing of X-ray cosmic background or an X-ray all-sky survey. We refer the reader at all the publications mentioned in this chapter.

## 3 Simulating the X-ray spectra

By simulating the X-ray spectra of baryon-sparse regions of the cosmic web, we wish to demonstrate the importance of new X-ray satellite missions. In this chapter, we will show how our spectra were obtained from Illustris TNG100-3 simulation, analysed and fitted. Fitting the spectra with models including background components may show whether the new X-ray observatories have the capabilities to resolve faint structures of the cosmic web or not.

### 3.1 Used packages

Nowadays, working with very complex data structures – such as cosmological simulation results – is not really handled by pen and paper. The everyday work of an astronomer requires much faster, stronger and more reliable methods. To process simulation data, to create mock observations with telescopes and instruments, to simulate spectra and to fit those spectra accordingly, we used various computational algorithms.

#### 3.1.1 pyXSIM

For simulating the X-ray emission based on the TNG simulation, we used the *pyXSIM Python* package (ZuHone; Hallman [48], 2016). *pyXSIM* is a tool, built by John ZuHone<sup>1</sup>, used to simulate X-ray events and photons from astrophysical sources and to create gas maps of hot regions. *pyXSIM* is heavily supported by the *yt* package developed by the *yt collaboration*<sup>2</sup> (39). In our workspace, we used *pyXSIM* version 4.3.2.

#### 3.1.2 SOXS

*SOXS* (ZuHone [49], 2023), Simulated Observations of X-ray Sources, is a *Python* package developed by scientists at CfA mainly to be used with the future X-ray mission concepts of LEM and Lynx. *SOXS* is an environment, where mock X-ray observations are conducted. It consists of a database of instruments and their parameters. *SOXS* is also a tool used for modelling background emission for observations including instrumental background and overall cosmic X-ray background. The resulting product of *SOXS* observations are mock event files from which full field of view (FOV) spectra can

---

1. John ZuHone is an astrophysicist and researcher at the Harvard-Smithsonian Center for Astrophysics (CfA) in Cambridge, USA.

2. The *yt* Project is a collaboration of many enthusiastic physicists at Open Hub. It aims to be a general tool to be used to simulate and visualise a range of various data structures.

be extracted as observed by various satellites. In our workspace, we used SOXS version 4.7.1.

#### 3.1.3 Xspec

*Xspec* (Arnaud [3], 1996) is a NASA's HEASARC<sup>3</sup> (14) HEASoft<sup>4</sup> tool used for spectral fitting. Its interface is terminal-based and because its base functions are very straightforward, it has been used by a wide range of scientists for over 35 years now. In our workspace, we used *Xspec* version 12.12.1.

## 3.2 Handling the simulation data

For the purposes of this thesis, we decided to use the TNG100-3 simulation – the 100 Mpc<sup>3</sup> volume of TNG, where massive structures (such as galaxy group halos) are formed. In between galaxy groups and clusters, thin gas of the WHIM-like temperatures can be found. Regarding data acquisition, all TNG simulations are available for download from the TNG web page archive (Nelson [27], 2019)<sup>5</sup>.

The loading of TNG data structure can be done in many ways, either by loading only a defined subset of data (such as halos or sub-halos) or by loading the whole snapshot at given redshift. For the purposes of demonstrating the capabilities of X-ray missions, we decided that the last snapshot with redshift  $z = 0.01$  is satisfactory. As we found for the most massive halo in TNG100 simulation, this region is full of interesting features. We decided to load this subset of simulation data:

```
1 basePath = "/space/IllustrisTNG/TNG100-3/output/"
2 snap = 99
3 haloID = 0
4 halo = il.groupcat.loadSingle(basePath, snap, haloID=haloID)
5
6 fields = ['Coordinates',
7           'GFM_CoolingRate',
8           'Density',
9           'InternalEnergy',
10          'ElectronAbundance',
```

---

3. The High Energy Astrophysics Science Archive Research Center is a NASA archive for high-energy related astrophysical research.

4. HEASoft is a complex software suite containing several packages for high-energy related astrophysical research. It includes FTOOLS/FV and XANADU (later divided into *Ximage*, *Xronos* and *Xspec*).

5. We acquired the TNG data set at (38).

```

11         'StarFormationRate']
12 gas = il.snapshot.loadHalo(basePath, snap, haloID, "gas")
13 header = il.groupcat.loadHeader(basePath, snap)
14
15 with h5py.File(il.snapshot.snapPath(basePath, snap), 'r') as f:
16     header_snap = dict(f['Header'].attrs)

```

After that, the data is loaded by yt (see the Appendix C and D for the whole code) and projection is centered at the center of selected halo, group or cluster. When searching for WHIM regions, center of projection must be shifted away from the group/cluster. This shift is easily performed:

```

1 ds = yt.load(filename)
2
3 c = ds.arr([
4     halo["GroupPos"][0],
5     halo["GroupPos"][1],
6     halo["GroupPos"][2]],
7     "code_length")           # Centered at selected halo
8
9 dx, dy, dz = 0.0, -50.0, 50.0 # Define shift values
10 c_shifted = ds.arr([
11     halo["GroupPos"][0] + dx,
12     halo["GroupPos"][1] + dy,
13     halo["GroupPos"][2] + dz],
14     "code_length")         # Center shifted

```

When centering at WHIM filaments, a hot gas filter is added to yt (see the Appendix C) and the search is performed by projecting this hot gas with `yt.ProjectionPlot`, such as:

```

1 prj = yt.ProjectionPlot(ds, "x", ("hot_gas", "density"),
2     ↪ width=(1, "Mpc"), center=c)
3 prj.set_zlim(("hot_gas", "density"), 1.0e-7, 1.0e-3)
4 prj.show()

```

When the center `c` is set accordingly, the model observation can be set with `pyXSIM` and mock observation can be configured with `SOXS`.

All cosmological parameters within the loaded snapshot are printed by default when loading a yt object and are shown in Table 3.1.

**Table 3.1:** All the cosmological parameters values used within the TNG100-3 simulation volume and used snapshot.

| Parameter                | Value                                      |
|--------------------------|--|
| $\Omega_\Lambda$         | 0.6911                                     |
| $\Omega_{\text{matter}}$ | 0.3089                                     |
| $\Omega_{\text{rad}}$    | 0.0  |
| Redshift                 | 0.0  |
| $H_0$                    | $67.74 \text{ km s}^{-1} \text{ Mpc}^{-1}$ |
| Current time             | $4.36 \times 10^{17} \text{ s}$            |

### 3.3 Instrument simulations

The most powerful tool of *SOXS* are undoubtedly its instrument simulations. The package creates mock observations of X-ray sources just given a dataset of events and photons. The method `soxs.instrument_simulator()` offers a range of observational parameters to be set.

#### 3.3.1 X-ray satellites: response files

Response files, or response matrices are calibration files used for calibrating observations – both real and simulated. They usually consist of a pair of files measuring the energy sensitivity and channel distribution. These are called the ancillary response file (ARF) and the redistribution matrix file (RMF).

The *ARF* is somehow similar to a measure of energy sensitivity of the detector when compared to infrared or optical astronomy. It is a dependence curve of effective area as a function of X-ray photon energy. Every piece of equipment in X-ray satellites, such as mirrors, spectrometers, filters or detectors, usually contributes to this generally non-constant distribution.

When an X-ray photon is detected by a satellite, it is (based on its energy) immediately designated an energy channel, where this information is stored. Sometimes it happens, that some photons may ‘fall’ into different channels than expected. This probability is reflected by the *RMF* matrix. Ideally, the *RMF* is a linear distribution (a matrix with diagonal terms only), but in reality it contains some second-order (and higher) contributions.

Usually other calibration files are provided by X-ray satellite collaborations. These include the background radiation file (often denoted *PHA* – Pulse Height Amplitude, a name, that still remained from *ancient* times, when proportional counters were used as X-ray detectors), mapping the instrumental background of the satellite and the Point-Spread Function (*PSF*), a measure of spatial photon distribution across the detector. The *PSF* is

**Table 3.2:** All the available parameters of `soxs.instrument_simulator()`.

| Argument  | Function   |
|---|--|
| <code>source_file</code>  | By default the first parameter. Selects a source file (usually a <i>pyXSIM</i> event list or SIMPUT catalog) from which the simulation data will be drawn.   |
| <code>out_file</code>   | Sets the name of output file.  |
| <code>exp_time</code>   | Sets exposition time of the mock observation.  |
| <code>instrument</code>   | Searches the instrument registry and selects an instrument of choice for which the X-ray source will be observed.  |
| <code>sky_center</code>   | Usually, within <i>pyXSIM</i> event list, the sky coordinates of observed source are set. By setting the <code>sky_center</code> coordinates accordingly, shifting the viewpoint of the satellite is possible. |
| <code>roll_angle</code>   | Sets the satellite angle (its rotation around source center) under which the observation is conducted.   |
| <code>ptsrc_bkgnd</code><br><code>instr_bkgnd</code><br><code>foreground</code> | Parameters needed to simulate all the background radiation. (more about simulating the background in the following sections). By default, all three are set to <i>True</i> .                                   |
| <code>dither_params</code>  | The dithering of the satellite can be set using this parameter. In case no dither is to be simulated, the <code>no_dither</code> parameter can be used instead.  |
| <code>aimpt_shift</code>  | By using this parameter, it is possible to shift the (otherwise) center of observation.  |

### 3. SIMULATING THE X-RAY SPECTRA

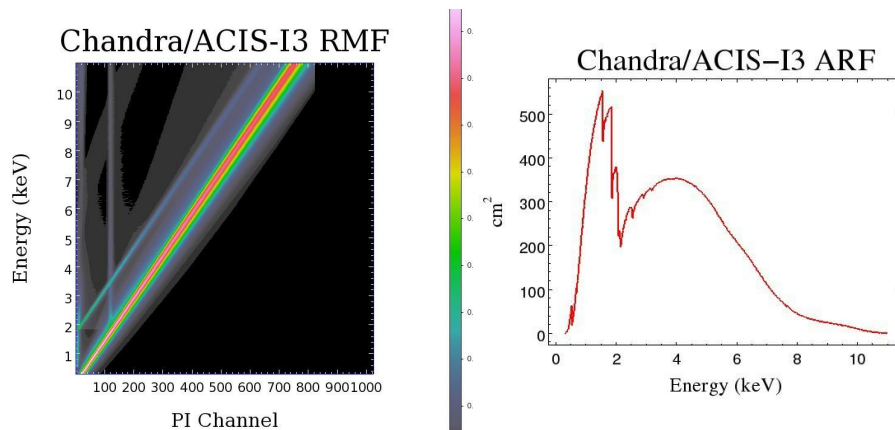


**Figure 3.1:** The Chandra RMF and ARF response matrices. Note the RMF non-diagonal elements, causing the same-energy photons to be sometimes detected in different channels (color refers to detection probability). Credit: *An X-ray Data Primer: What I Wish I Knew when Starting X-Ray Astronomy* [2]

a somewhat complex matrix, binding together photon energy, actual spatial distribution of the source, mirror geometry and distance of the source from the center of the satellite’s field of view. For example, when observing an X-ray point-like source on the edge of field of view, it does usually spatially spread out. The reconstruction of such source is then very difficult.

Most of the response files are usually publicly available, for example, we can obtain them via *SOXS* or at a web archive. Acquiring response files via *SOXS* is very simple. The *SOXS* package comes with a method `soxs.fetch_files()` with the only required parameter being the name of the respective X-ray instrument we wish to obtain files for. This command then downloads respective files (used by *SOXS*) from a web archive to current folder. The following Table 3.3 shows the list of response files we used within the simulations.

We acquired the response files used through various methods. Files for Chandra (cycle 22) were obtained directly via the `soxs.fetch_files()` method and downloaded into our workspace from a *SOXS* web archive. The same method of acquisition was used with files of LEM and XRISM satellites. As for the NewAthena, we downloaded their newest response files at the web page of the Athena collaboration (4). The HUBS response files were not publicly available. We obtained the HUBS ARF and RMF directly via asking the HUBS collaboration. With this being said, I wish to thank the collaboration for handing in all the files necessary without hesitation.



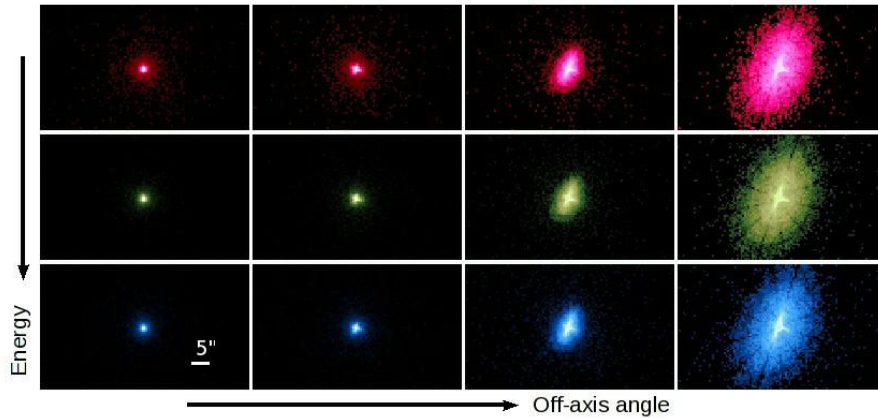


**Figure 3.2:** The effect of PSF, the Point Spread Function when observing X-ray sources off-axis with Chandra X-ray Observatory. See how is the point source spread across the detector with increasing energy (0.92, 1.56 and 3.8 keV) and off-axis angle (0, 2.4, 4.7 and 9.6 arcmin). Credit: *An X-ray Data Primer: What I Wish I Knew when Starting X-Ray Astronomy* [2]

**Table 3.3:** List of all response files used and corresponding satellites.

| Response file                                   | Satellite | Type            |
|---|-----------|-----------------|
| <i>aciss_aimpt_cy22.rmf</i>                     | Chandra   | RMF             |
| <i>aciss_aimpt_cy22.arf</i>                     | Chandra   | ARF             |
| <i>chandra_aciss_cy22_bi_particle_bkgnd.pha</i> | Chandra   | Background file |
| <i>resolve_h5ev_2019a.rmf</i>                   | XRISM     | RMF             |
| <i>resolve_pnt_heasim_noGV_20190701.arf</i>     | XRISM     | ARF             |
| <i>resolve_h5ev_2019a_rslnxb.pha</i>            | XRISM     | Background file |
| <i>athena_xifu_3eV_gaussian.rmf</i>             | NewAthena | RMF             |
| <i>athena_xifu_13_rows_no_filter.arf</i>        | NewAthena | ARF             |
| <i>athena_psf_defoc_20231211.fits</i>           | NewAthena | Background file |
| <i>lem_1.3eV_110422.rmf</i>                     | LEM       | RMF             |
| <i>lem_300522.arf</i>                           | LEM       | ARF             |
| <i>lem_1.3eV_171222_fov_bkg.pi</i>              | LEM       | Background file |
| <i>hubs_cc_s_v20181130.rmf</i>                  | HUBS      | RMF             |
| <i>hubs_cc_s_v20201227.arf</i>                  | HUBS      | ARF             |

### 3.3.2 Adding custom instruments

The lack of some instruments or their parameters in *SOXS instrument\_registry* led me to update it manually. The HUBS mission was not present among *SOXS* instruments, so we had to add it into the registry and include all response files necessary for it to work along with our code.

To add custom instruments along with all the necessary response files into the *SOXS* registry, a sophisticated method *add\_instrument\_to\_registry()* is implemented within *SOXS*. A little less complicated method, that we used to create a new instruments and instrument specifications is updating the registry directly, since it is only an editable *Python* script. This instrument registry can be by default (for Linux and anaconda users) found at *home/yourname/anaconda3/envs/envname/lib/python3.11/site-packages/SOXS*, where *yourname* represents the Linux username and *envname* the name of a respective anaconda environment, where *SOXS* is installed. We proceeded to edit the script by copying an existing instrument and rewriting its parameters to best represent the HUBS satellite. With this setup, we decided to ignore the instrumental background (thought not to be relevant in comparison to all the other background components) and to represent the point-spread function as a simple Gaussian profile with a width of 1 arcsec.

```
1 # HUBS --- my own HUBS
2
3 instrument_registry["hubs"] = {
4     "name": "hubs",
5     "arf": "hubs_cc_s_v20201227.arf",
6     "rmf": "hubs_cc_s_v20181130.rmf",
7     "bkgnd": None,
8     "fov": 60.0,
9     "num_pixels": 600,
10    "aimpt_coords": [0.0, 0.0],
11    "chips": [["Box", 0, 0, 60, 60]],
12    "focal_length": 5.0,
13    "dither": True,
14    "psf": ["gaussian", 1.0],
15    "imaging": True,
16    "grating": False,
17 }
```

For this to work properly, all the respective response files need to be stored in *SOXS* cache located by default at *home/yourname/.cache/soxs*.

For simulating observations with Athena, a similar approach was needed, because response files used by *SOXS* were too outdated. After obtaining

newest response files from (4), we reworked the instrument registry by copy-pasting the Athena instrument, renaming it and rewriting the 'rmf', 'arf', 'bkgnd' and 'psf' key values to the respective filenames of new response matrices.

```

1 # NewAthena XIFU --- my own Athena
2
3 instrument_registry["NewAthena"] = {
4     "name": "NewAthena",
5     "arf": "athena_xifu_13_rows_no_filter.arf",
6     "rmf": "athena_xifu_3eV_gaussian.rmf",
7     "bkgnd": ["athena_xifu_nxb_10asec_radius.pha",
8     ↪ 79552.92570677],
9     "fov": 5.991992621478149,
10    "num_pixels": 84,
11    "aimpt_coords": [0.0, 0.0],
12    "chips": [{"Polygon", [-33, 0, 33, 33, 0, -33], [20, 38, 20,
13    ↪ -20, -38, -20]}],
14    "focal_length": 12.0,
15    "dither": True,
16    "psf": ["multi_image", "athena_psf_defoc_20231211.fits"],
17    "imaging": True,
18    "grating": False,
19 }

```

Similarly to handling HUBS response files, we uploaded the newest Athena files to proper default directory, so that SOXS can use them. All the other instruments were already present in SOXS instrument registry with response matrices enough up to date.

### 3.3.3 Simulating background radiation

SOXS offers a complex way to simulate X-ray background events directly within the `soxs.instrument_simulator()` method. By default, SOXS simulates three types of background (see Table 3.4): the Galactic foreground, cosmic X-ray background (CXB) and the instrumental background. The most important of those are the Galactic foreground and point-source background. Because instrumental background is generally negligible in comparison to the other sources when observing with a calorimeter, we can safely ignore it regarding the aim of this thesis (except for the Chandra X-ray Observatory).

The Galactic foreground consists of two components: the local hot bubble and hot halo (see Fig. 1.4). Both are in SOXS by default modelled by a thermal model

### 3. SIMULATING THE X-RAY SPECTRA

$$\text{apec}_{\text{LHB}} + \text{phabs}(\text{apec}_{\text{GH}}),$$

with the parameters values shown in Table 3.4<sup>6</sup>.

The CXB represents emission noise originating from distant point sources such as AGN or galaxies. The CXB background is simulated using discrete point sources distributed randomly during the simulation and each is given a power-law spectrum. More details on simulating background models with SOXS can be found at *SOXS: Simulated Observations of X-ray Sources* [34].

**Table 3.4:** Galactic foreground models parameters in SOXS. Credit: SOXS: *Simulated Observations of X-ray Sources* [34]

| Model:   | phabs (apec <sub>LHB</sub> )  | apec <sub>GH</sub>  |
|----------|---|---|
| nH       | $0.018 \times 10^{22} \text{ cm}^{-2}$  | -   |
| kT       | 0.225 keV   | 0.099 keV   |
| abund    | $1.0 Z_{\odot}$   | $1.0 Z_{\odot}$   |
| redshift | 0.0   | 0.0   |
| norm     | $7.3 \times 10^{-8} \times 10^{-14} \frac{\int n_e n_H dV}{4\pi D_A^2 (1+z)^2}$ | $1.7 \times 10^{-7} \times 10^{-14} \frac{\int n_e n_H dV}{4\pi D_A^2 (1+z)^2}$ |

#### 3.3.4 Configuration of observations

Following all the steps above in this chapter, we arrived at creating *pyXSIM* model observations of selected sources. The *pyXSIM* package offers configuration of a thermal CIE source model with its function *pyxsim.CIESourceModel()*. For our setup, a yt hot gas filter was defined in advance by restricting the temperature, star formation rate and cooling rate parameters within our dataset. The source model was then defined based on the hot gas filter and a temperature range in keV as follows:

```

1 source_model = pyxsim.CIESourceModel(
2     "apec", emin, emax, nbins, ("hot_gas", "metallicity"),
3     temperature_field=("hot_gas", "temperature"),
4     emission_measure_field=("hot_gas", "emission_measure"))

```

Based on the created CIE model, simulated emission from a selected box could be drawn using *pyxsim.make\_photons()* and *pyxsim.project\_photons()*

6. *Apec*, the Astrophysical plasma emission code is a widely used model for simulating hot X-ray emitting gas. It consists of several components (as can be seen in the mentioned Table 3.4). The *phabs*, photon electric absorption on gas within our own Galaxy, is an absorption model.

functions. Note that projecting photons in *pyXSIM* naturally requires an axis of projection as an argument. If we wish to project under an axis rotation, an array must be used instead. The following code demonstrates how we could project photons in different directions, which was useful when searching for the most suitable observation angle. The first example shows the default use of the projecting function, the second a rotated version. The code includes the well known *numPy Python* package.

```

1  # Original projection along "x" axis
2  n_events = pyxsim.project_photons(f"halo_{haloID}_photons",
3                                   f"halo_{haloID}_events", "x", (45.,30.),
4                                   absorb_model="wabs", nH=0.01)
5
6  # A random rotation along projection axis
7  original_axis = np.array([1, 0, 0])
8  ang_x = 45
9  ang_y = 20
10 ang_z = 0
11
12 r_x = R.from_rotvec(np.radians(ang_x) * np.array([1, 0, 0]))
13 r_y = R.from_rotvec(np.radians(ang_y) * np.array([0, 1, 0]))
14 r_z = R.from_rotvec(np.radians(ang_z) * np.array([0, 0, 1]))
15
16 rotated_axis = r_z.apply(r_y.apply(r_x.apply(original_axis)))
17
18 n_events = pyxsim.project_photons(f"halo_{haloID}_photons",
19                                   f"halo_{haloID}_events", rotated_axis, (45.,30.),
20                                   absorb_model="wabs", nH=0.01)

```

As a next step, a *pyXSIM* event list and a simput catalog are created, from which mock observations and spectra are obtained.

### 3.3.5 Mock observations and spectra

All mock observations of X-ray sources simulated within TNG100 and modelled by yt and *pyXSIM* are created by SOXS with *soxs.instrument\_simulator()*. Finally, after projecting hot gas emission into an event list, observations of a source are done simply by convolving projection data with individual satellite response files and its field of view, given an exposure time and simulated background option. One-dimensional spectra are acquired with *soxs.write\_spectrum()*. The output is typically a *.pi* file with the spectrum. Raw full FOV spectra obtained with SOXS need to be fitted with a spec-

tral fitting tool, since inside them resides the most scientifically valuable information.

### 3.4 Spectral fitting with *Xspec*

As was stated above, the X-ray spectrum of the hot intergalactic gas is composed of various different components. Apart from the WHIM region itself, the background radiation contributes to it significantly. There are technically two ways of how to tell if a satellite spectrometer/microcalorimeter is able to resolve the hot gas region from the background radiation.

The less scientific approach is done by simulating emission from thin regions without background radiation completely and then overviewing the whole spectrum itself. If there is no significant detection, or the number of detected source counts is extremely low, we can safely label the region undetectable. If there is, however, any sign of X-ray photon detection, the simulation must be repeated with simulated background events and the resulting spectrum must be fitted to tell the significance of the detection.

To fit the resulting X-ray spectrum, we used the *Xspec* tool. *Xspec* runs in an open terminal and an external widow can be used to visualize the data. First, loading of the data is done using the `load path/to/file.pi` command, which loads the given spectrum and the respective response matrices. Usually, there is no need to use more commands for response files loading, since if they are present in the local directory, *Xspec* loads them automatically.

Next, we proceeded to the creation of a fitting model. According to the background model form *SOXS*, for the full model, we used

$$\text{apec}_{\text{LHB}} + \text{phabs}(\text{apec}_{\text{GH}}) + \text{phabs}(\text{apec} + \text{powerlaw}_{\text{CXB}}),$$

with the parameters (such as temperature or redshift) corresponding to the model parameters in Table 3.4 and the last two terms representing the hot gas component itself and the unresolved point source X-ray background. In cases, where the `powerlaw` photon index could be fitted, we used the value of 1.5 as a default starting point. For the `phabs` model, the *bcmc* cross-section was assumed (Balucinska-Church [5], 1992) and abundances were expressed with respect to proto-Solar abundances Lodders [21], 2009.

The initial parameters of the hot gas component were set according to the values drawn from the simulation volume. The fitting itself was then done by thawing and fitting the background component normalisations first, then fitting the hot gas component parameters one by one along with the background normalisations. Note that the Cash-statistic (Cash [8], 1979), set with the command `statistic cstat`, was used to fit all simulated spectra.

In some cases, beside the normalisation itself, we also tried estimating the temperature of selected region, or its abundance (metallicity). Furthermore, the photon index can also be constrained mainly with satellites able to resolve spectra over 2.0 keV.

#### **3.4.1 Data analysis**

The final data analysis is done with *Xspec* fitting results. The uncertainties are obtained via the *error* command. In some cases, the data are not sufficient to constrain parameters of all fitted components (e.g. only upper limits can be estimated). We may inspect the relevance of given fits also by fitting the data only with the background components (searching if adding the *apec* component provides a better fit than fitting just the background model). The respective results are discussed in the next chapter.





## 4 Results

By simulating mock observations of a cluster halo and a baryon-sparse region within the TNG100-3 simulation with next-generation X-ray instruments, we were trying to figure out whether the regions are observable by a given instrument and, if so, how significant this WHIM/ICM/IGM detection would be. We chose five distinct regions. The first three are the halo center,  $r_{500}$  region and  $r_{200}$  region<sup>1</sup>, since the values of  $r_{500}$  and  $r_{200}$  are easily obtained directly from TNG halo database. For comparison, it is often stated that current X-ray missions are able to observe cluster/group halos approximately up to  $r_{200}$ . The respective distances of the two chosen regions from cluster center are 437 and 696 kpc. To show the ability of missions of the future, two more regions were selected. One still belonging to the cluster halo beyond  $r_{200}$ , 889 kpc from the center, and one 2.96 Mpc away, representing (by its physical description) a filament-like structure. All the regions are visualised in Figure 4.1.

All of our simulated regions were situated at fixed redshift  $z = 0.01$  and with absorbing Galactic hydrogen column  $n_{\text{H}} = 0.01 \times 10^{22} \text{ cm}^2$ . All uncertainties are expressed within  $1\sigma$  (68.3%) confidence level.

### 4.1 Halo center

The region in the very center of the selected massive halo was simulated with a 10 ks exposure time with all of our instruments. This region is the hottest and densest region, with average density of  $(2.0 \pm 0.4) \times 10^{-2} \text{ cm}^{-3}$ .

As can be seen from the resulting fits (see Figures 4.2, B.1, B.2 and Table A.1), this region is easily recognized by every instrument that we used. Even from the Chandra ACIS-S CCD and the usually photon-starved XRISM Resolve spectra, the local component normalisation and temperature can be determined with high enough accuracy. This result was expected as the number of photons detected by the satellites was sufficiently high and the hot gas component dominated over all the simulated background components.

Since the hot gas component at given high temperature dominates over the *powerlaw* spectrum, it is only natural, that the *powerlaw* component could not be distinguished within any of the spectra. We fitted this component only to demonstrate this fact. Otherwise, when fitting spectra of actual

---

1. These stand for the halo radii, where the total gas density (computed simply as total baryonic mass divided by local volume given by the radius  $r$ ) reaches 200 or 500 times the cosmological critical density.

## 4. RESULTS

---

observations, the *powerlaw* component is not fitted in such regions. Full fit results along with spectra can be found in the Appendix A and B.

As can be seen in Figure 4.2, this was the only region, we were able to fit properly with Chandra ACIS-S. In the remaining regions, the instrumental background of ACIS-S CCD detector started to dominate over the spectrum and the spectral fits became inaccurate. Therefore, we did not simulate spectra further away from the halo center with Chandra ACIS-S.

### 4.2 Halo $r_{500}$

Going further away from the center, the hot  $r_{500}$  region was observed with 100 ks exposure time. The average number density of this particular region was  $(3.6 \pm 1.3) \times 10^{-3} \text{ cm}^{-3}$ .

The hot gas component in a region centered at  $r_{500}$  of the selected halo was again distinguished from the background radiation by all of the used instruments excluding Chandra ACIS-S, where the instrumental background dominated the spectrum. We can only comment on the wide temperature range fitted within virtually all of the spectra. This divergence was likely a product of two distinct temperature populations in our sample, as can be seen in Fig. 4.4. The inability of some instruments to fit the *powerlaw* normalisation properly in this region is again driven by the same means as it was commented earlier in the central region. Full fit results along with spectra can be found in the Appendix A and B.

### 4.3 Halo $r_{200}$

At the current theoretical border of detection capability, in the region of  $r_{200}$ , the average number density of particles was  $(1.1 \pm 0.3) \times 10^{-3} \text{ cm}^{-3}$ .

Simulating this region, the XRISM Resolve detection was already very faint and no hot gas component was found within it. This can be seen in Table A.3. The *powerlaw* spectrum now started to dominate over all the other components, so it could be fitted well with all of the used instruments. Regarding the detections with NewAthena X-IFU, HUBS and LEM IFU, all of these new missions were still able to resolve the hot gas component within their respective spectra with high enough accuracy. Full fit results along with spectra can be found in the Appendix A and B.

#### 4.4 Halo beyond $r_{200}$

Beyond the current observable horizon of  $\sim r_{200}$ , we simulated spectra for all microcalorimeter instruments with 100 ks exposure time. With the HUBS satellite we also created one 1 Ms observation for comparison with the 100 ks spectra (the HUBS collaboration is planning to schedule such long-exposure measurements). This region was characterised by the average particle concentration of  $(6.5 \pm 1.4) \times 10^{-4} \text{ cm}^{-3}$ .

By simulating and fitting spectra of the halo outskirts, 889 kpc from the center of selected massive halo, we obtained results summarized in Table A.4. For XRISM Resolve, the hot gas emission is almost (or totally) non-detectable. Because XRISM (along with Chandra) could not significantly resolve the hot gas component even at  $r_{200}$ , their failure to do so in a less dense region is not very surprising.

The NewAthena mission, along with the HUBS and the LEM satellite did all distinguish the hot gas component within their spectra. From the fitting results in Table A.4, we can see, that all the normalisation fits are significant enough. When fitting the HUBS 1 Ms exposure time spectrum, we obtained even better results in terms of the average temperature determination.

#### 4.5 WHIM filament

The results for simulating spectra of a filament-like region of the WHIM are summarised in this section. All the mock observations were again simulated with an exposure time of 100 ks with the exception of HUBS and LEM satellites, where a 1 Ms observation was also simulated. The average number density of the filament region was  $(7.3 \pm 2.1) \times 10^{-5} \text{ cm}^{-3}$ .

As can be seen from the spectrum in Fig. 4.8 and from the resulting fits in Table 4.1, XRISM Resolve was not able to resolve the WHIM filament at all. A 100 ks exposure time is not enough for XRISM to detect enough X-ray photons to sufficiently resolve any hot gas component.

Some of the finer spectra were fitted separately with and without the filament component to observe whether the detections are statistically better or worse. From the remaining plots and fits (see Figures 4.8, 4.9, 4.10 and Table 4.1), we can see that NewAthena satellite is not able to resolve the WHIM gas component in the spectrum. The detection is rather weak and the margin of error virtually exceeds the value fitted itself, or is too large for the detection to be considered relevant. When fitting only the background components, NewAthena produces a fit almost indistinguishable from the result obtained when fitting with hot gas component. The HUBS mission was however more successful in detecting the WHIM filament. As we can

observe, even the 100 ks observation of HUBS has detected the emission of the filament and also allowed estimating its temperature. From the obtained C-statistics in Table 4.1, we can see that for both 100 ks and 1 Ms observations, including the component for the WHIM emission significantly improves the fit statistics. Regarding the LEM satellite, the hot gas detection for 100 ks exposure time is very faint, however it is visible in the resulting fit and statistically preferred. The 1 Ms simulated spectrum fit results for the LEM satellite are even more promising, with the hot gas component being recognised very well.

### 4.6 Data availability

Regarding our data analysis, we wish to be transparent. The full code along with the resulting raw spectra and plots of spectra used in this thesis are available at [github.com/madmad02/Bc-Thesis\\_XRS\\_public](https://github.com/madmad02/Bc-Thesis_XRS_public), in a public GitHub repository. The reader is encouraged to explore our results.

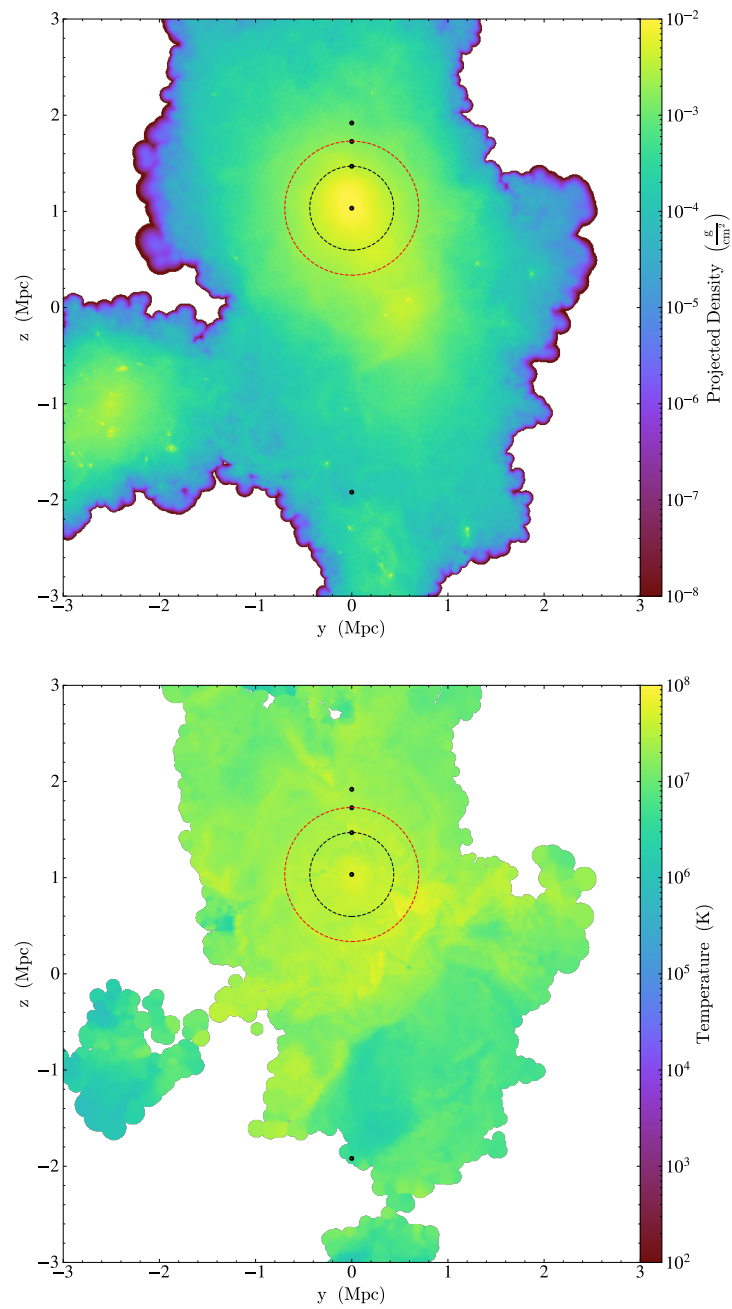


**Figure 4.1:** All the observed regions around selected halo: the halo center,  $r_{500}$  and  $r_{200}$  regions, a less dense region beyond  $r_{200}$  and a filament-like WHIM region, all marked by black dots. A total gas density projection (top) and a temperature slice (bottom). The  $r_{500}$  and  $r_{200}$  regions are marked by a black and a red circles.

## 4. RESULTS

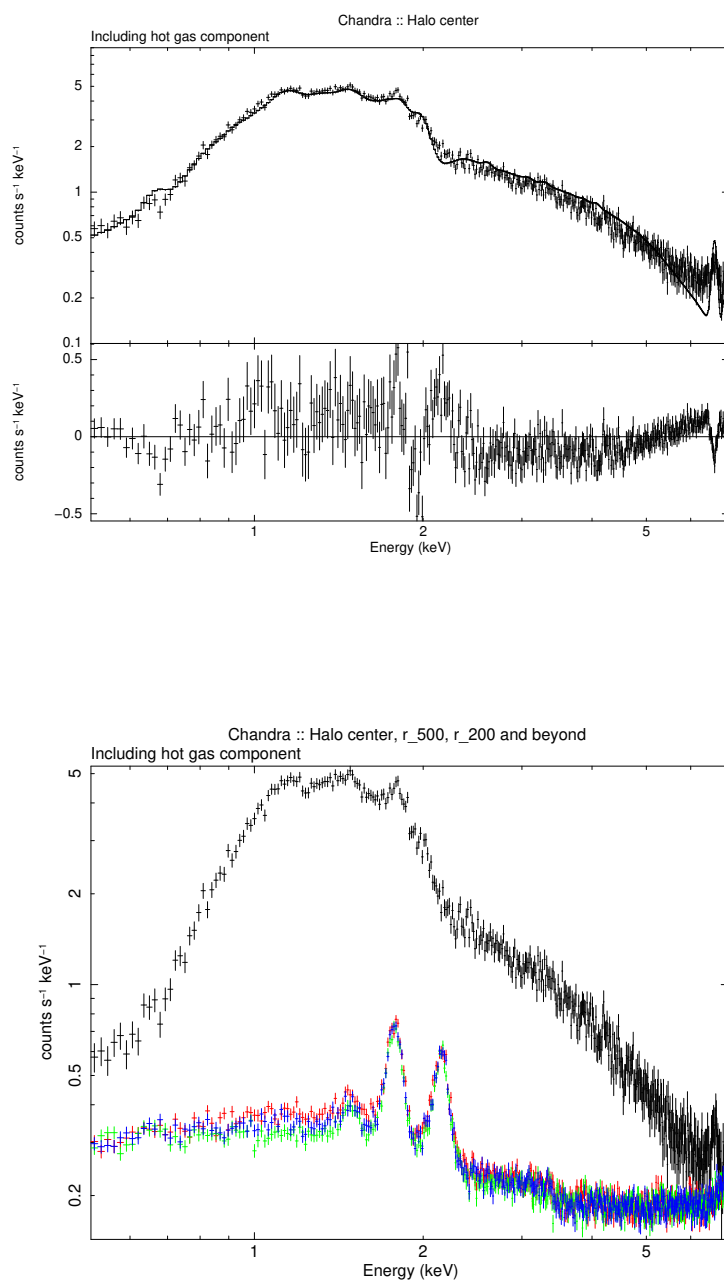


**Figure 4.2:** Fitted spectra of the halo center region along with fit residua with Chandra ACIS-S (top) and a plot of Chandra observations of halo center (black), halo  $r_{500}$  (red),  $r_{200}$  (blue) and the halo beyond  $r_{200}$  (green) regions. We can observe, that from the  $r_{500}$  region onward, ACIS-S spectra are dominated by instrumental background radiation.

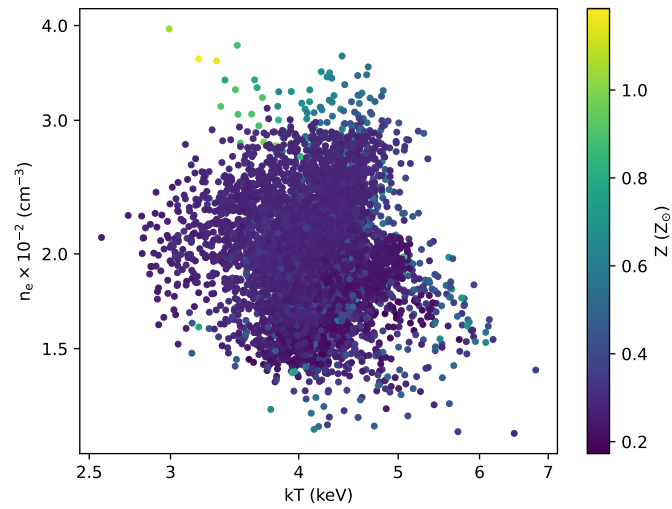


**Figure 4.3:** Distribution of the temperatures and electron densities of individual super-particles within the simulated box for halo center region. The color of individual particles refers to their abundance.

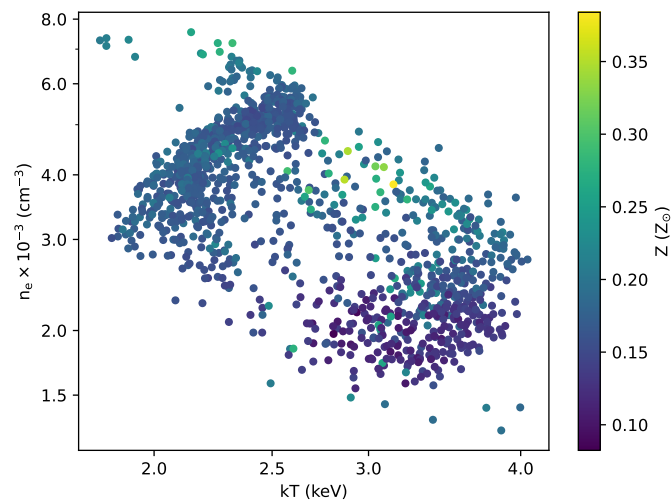


**Figure 4.4:** Distribution of the temperatures and electron densities of individual super-particles within the simulated box for the halo  $r_{500}$  region. The color of individual particles refers to their abundance.

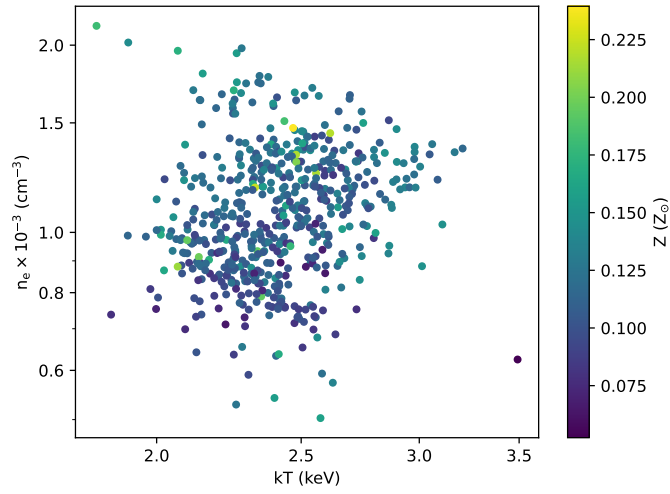


**Figure 4.5:** Distribution of the temperatures and electron densities of individual super-particles within the simulated box for the halo  $r_{200}$  region. The color of individual particles refers to their abundance.

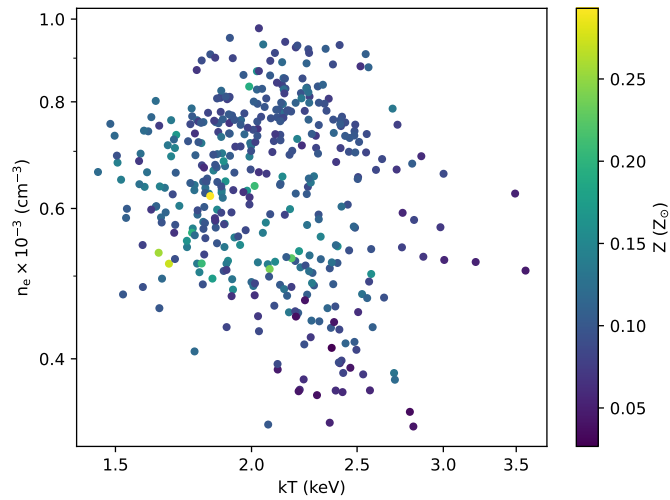


**Figure 4.6:** Distribution of the temperatures and electron densities of individual super-particles within the simulated box for the region beyond  $r_{200}$ . The color of individual particles refers to their abundance.



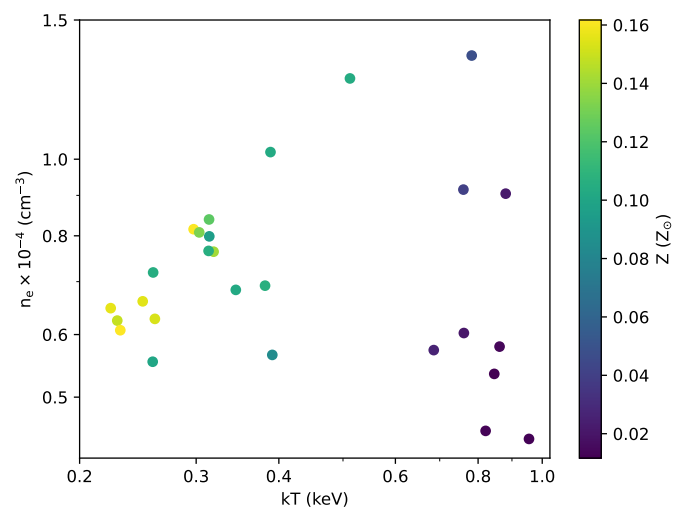


**Figure 4.7:** Distribution of the temperatures and electron densities of individual super-particles within the simulated box for the filament-like WHIM region. The color of individual particles refers to their abundance.

## 4. RESULTS

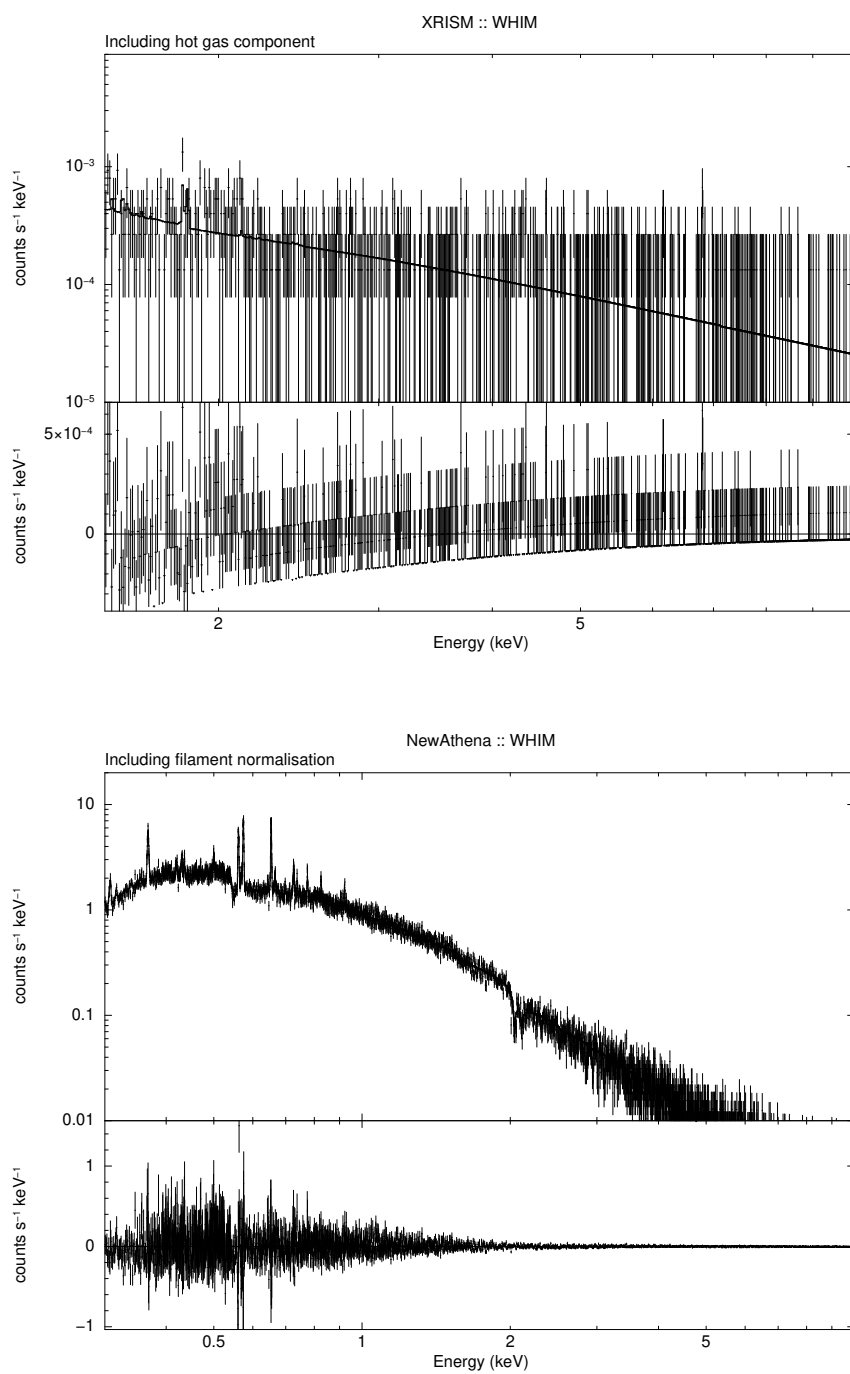


**Figure 4.8:** Fitted spectra of the WHIM filament along with fit residua with XRISM Resolve (top) and NewAthena X-IFU (bottom).

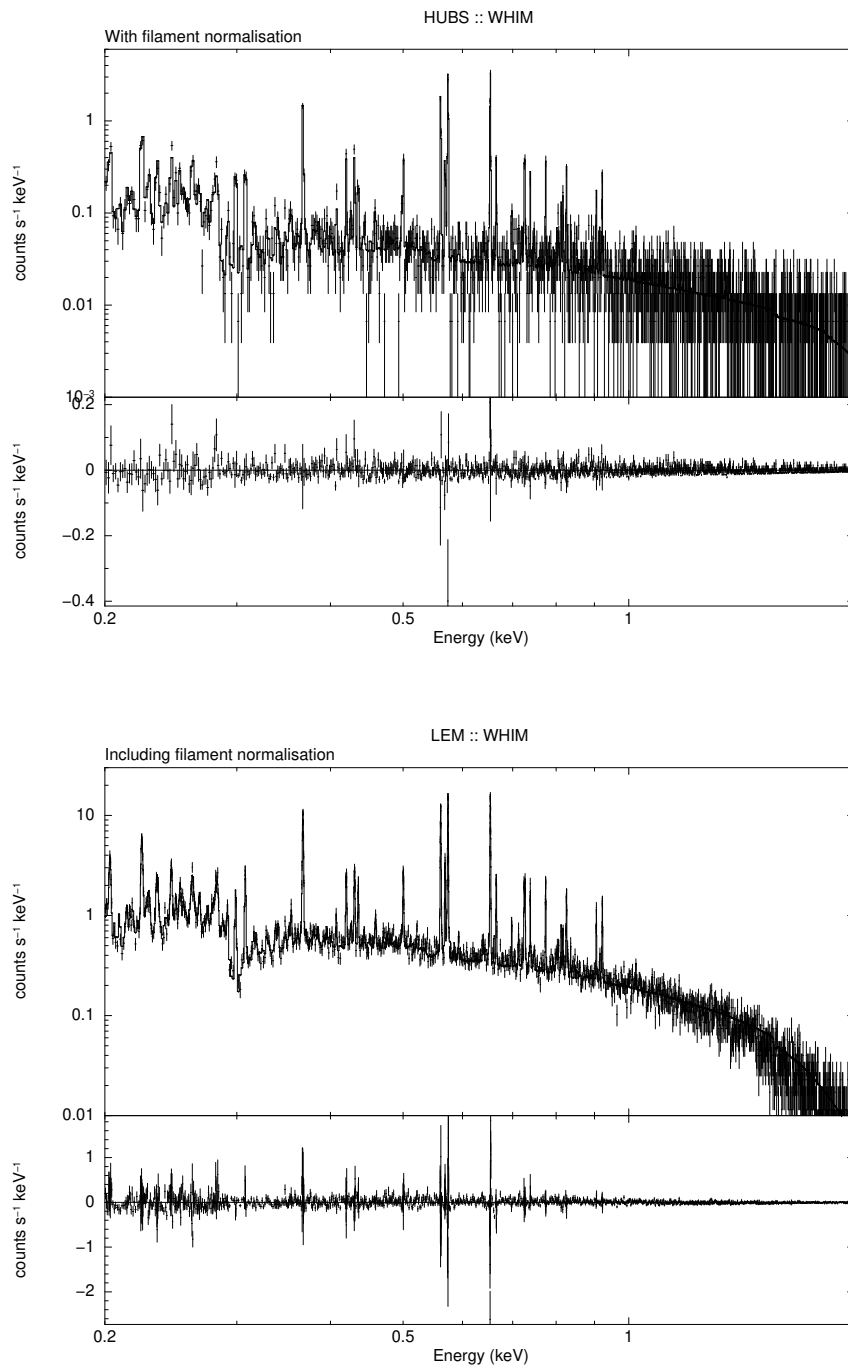


**Figure 4.9:** Fitted spectra of the WHIM filament along with fit residua with HUBS (top) and LEM IFU (bottom), both simulated with a 100 ks exposure time.

## 4. RESULTS

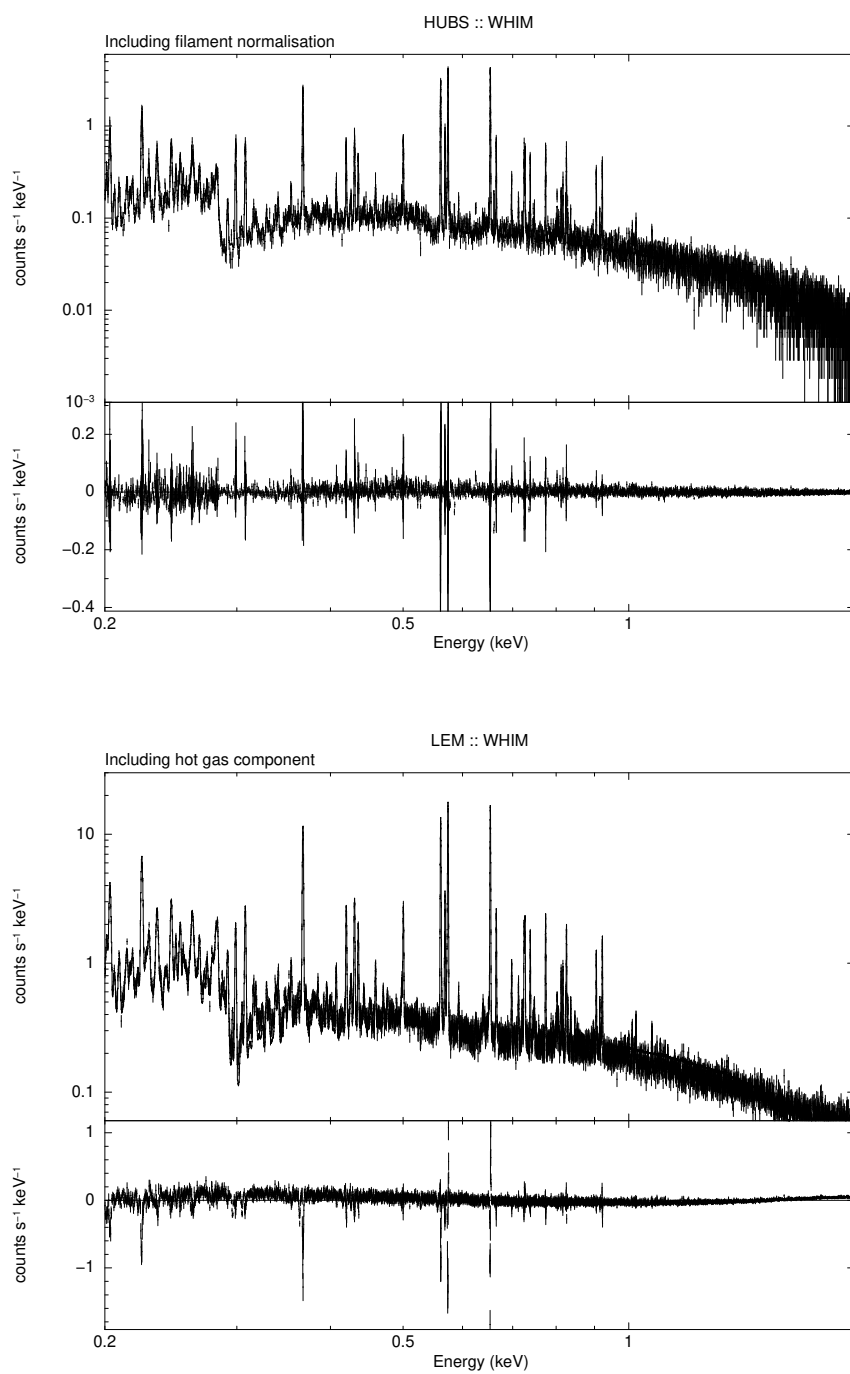


**Figure 4.10:** Fitted spectra of the WHIM filament along with fit residua with HUBS (top) and LEM IFU (bottom), a 1 Ms exposure time simulation.

Table 4.1: Resulting fitted parameters of filament-like WHIM region.

| Instrument            | Fit method | Background components            |                                  |                                    |                     |                                       | Photon index                          | Normalisation                  | Gas component |  | Statistic |
|-----------------------|------------|----------------------------------|----------------------------------|------------------------------------|---------------------|---------------------------------------|---------------------------------------|--------------------------------|---------------|--|-----------|
|                       |            | <i>apec</i>                      | <i>plabs*apec</i>                | <i>powerlaw</i>                    | Temperature (keV)   | Abundance                             |                                       |                                | Cstat/DOF     |  |           |
| XRISM                 | bkg+apec   | -                                | -                                | $(8.3 \pm 0.9) \times 10^{-4}$     | $1.48 \pm 0.07$     | $< 1.67 \times 10^{-5}$               | $< 2.2$                               | $9.1 \times 10^{-2}$           | 3048/16993    |  |           |
|                       | bkg+apec   | $(3.20 \pm 0.10) \times 10^{-5}$ | $(1.40 \pm 0.03) \times 10^{-5}$ | $(1.481 \pm 0.004) \times 10^{-4}$ | $2.175 \pm 0.004$   | $< 1.4 \times 10^{-6}$                | $0.37^{+0.22}_{-0.14}$                | $9.1 \times 10^{-2}$           | 16467/21832   |  |           |
|                       | bkg only   | $(3.22 \pm 0.10) \times 10^{-5}$ | $(1.40 \pm 0.03) \times 10^{-5}$ | $(1.481 \pm 0.004) \times 10^{-4}$ | $2.175 \pm 0.004$   | -                                     | -                                     | -                              | 16467/21835   |  |           |
| HUBS <sub>100ks</sub> | bkg+apec   | $(5.91 \pm 0.15) \times 10^{-5}$ | $(2.65 \pm 0.08) \times 10^{-5}$ | $(2.26 \pm 0.05) \times 10^{-5}$   | $1.7 \pm 0.2$       | $1.4^{+1.1}_{-1.0} \times 10^{-5}$    | $0.49 \pm 0.32$                       | $9.1 \times 10^{-2}$           | 11919/17993   |  |           |
|                       | bkg only   | $(5.81 \pm 0.15) \times 10^{-5}$ | $(2.56 \pm 0.07) \times 10^{-5}$ | $(1.41 \pm 0.06) \times 10^{-5}$   | $0.71 \pm 0.11$     | -                                     | -                                     | -                              | 12917/17995   |  |           |
| HUBS <sub>1Ms</sub>   | bkg+apec   | $(5.94 \pm 0.05) \times 10^{-5}$ | $(2.65 \pm 0.03) \times 10^{-5}$ | $(5.58 \pm 0.03) \times 10^{-5}$   | $1.973 \pm 0.009$   | $1.4^{+0.8}_{-0.7} \times 10^{-5}$    | $0.23^{+0.05}_{-0.03}$                | $9.1 \times 10^{-2}$           | 19706/17993   |  |           |
|                       | bkg only   | $(6.09 \pm 0.05) \times 10^{-5}$ | $(2.59 \pm 0.03) \times 10^{-5}$ | $(4.77 \pm 0.03) \times 10^{-5}$   | $1.768 \pm 0.011$   | -                                     | -                                     | -                              | 27932/17995   |  |           |
| LEM <sub>100ks</sub>  | bkg+apec   | $(8.01 \pm 0.11) \times 10^{-5}$ | $(3.59 \pm 0.05) \times 10^{-5}$ | $(7.40 \pm 0.06) \times 10^{-5}$   | $1.9721 \pm 0.0014$ | $3.1^{+8.3}_{-2.7} \times 10^{-5}$    | $0.33^{+0.11}_{-0.07}$                | $9.1 \times 10^{-2}$           | 7459/7193     |  |           |
|                       | bkg only   | $(8.23 \pm 0.10) \times 10^{-5}$ | $(3.59 \pm 0.05) \times 10^{-5}$ | $(6.48 \pm 0.06) \times 10^{-5}$   | $1.84 \pm 0.02$     | -                                     | -                                     | -                              | 9614/7195     |  |           |
| LEM <sub>1Ms</sub>    | bkg+apec   | $(9.29 \pm 0.04) \times 10^{-5}$ | $(3.79 \pm 0.02) \times 10^{-5}$ | $(8.26 \pm 0.02) \times 10^{-5}$   | $1.038 \pm 0.007$   | $1.66^{+0.17}_{-0.11} \times 10^{-4}$ | $7.28^{+0.11}_{-0.18} \times 10^{-2}$ | $9.1 \times 10^{-2}$           | 30676/7193    |  |           |
|                       | bkg only   | $(9.72 \pm 0.03) \times 10^{-5}$ | $(3.82 \pm 0.02) \times 10^{-5}$ | $(7.01 \pm 0.02) \times 10^{-5}$   | $0.537 \pm 0.009$   | -                                     | -                                     | -                              | 52799/7195    |  |           |
| Region parameters     |            | -                                | -                                | -                                  | -                   | -                                     | $0.48 \pm 0.24$                       | $(9.1 \pm 5.0) \times 10^{-2}$ | -             |  |           |



## 5 Conclusion

By simulating observations of multiple regions within the cosmic web with the X-ray satellites of today (the Chandra X-ray Observatory and XRISM) and of the future (NewAthena, HUBS and LEM), we were trying to determine the actual observational capabilities of all the missions. For our analysis, we chose a massive cluster halo and its outskirts from the Illustris TNG100-3 cosmological simulation. We simulated observations of five regions in total: the center of selected cluster, two regions at the distance of  $r_{500}$  and  $r_{200}$  from the center, one region at the very edge of the cluster halo and one region with WHIM-like properties, far away from the halo center. To conduct simulated observations and fit the resulting spectra, the *pyXSIM*, *yt* and *SOXS Python* packages and the *Xspec* fitting tool were used.

In the subsequent analysis of our results, spectra were fitted with a complex model including background components from the local hot bubble, Galactic halo, cosmic X-ray background, and the hot gas component itself. As expected, the hot gas component in halo center region was well recognised by all used instruments as can be seen in Table A.1. The  $r_{500}$  region was only non-detectable for Chandra ACIS-S. The fitting results are shown in Table A.2. The fitted spectra can be found in Figures 4.2, B.1 B.2, B.3 and B.4. The current missions with CCD spectral resolution have already shown their capabilities and the missions of the future are expected to have even better resolution.

This was further demonstrated by simulating a 100 ks exposure time spectra of the less dense regions. The halo  $r_{200}$  region was on the very edge of detection ability for XRISM Resolve, while all other TES-microcalorimeter designed instruments could still resolve the hot gas component with high enough confidence. All the results for the  $r_{200}$  region can be found in Table A.3 and fitted spectra in Figures B.5 and B.6.

The abilities of the next-generation X-ray missions were probed by simulated observations of a region further away from the center, where the average number density of particles was  $(6.5 \pm 1.4) \times 10^{-4} \text{ cm}^{-3}$ . While XRISM Resolve was unable to detect any significant hot gas component, NewAthena X-IFU, HUBS and LEM IFU all reported a significant detection within their spectra even with only a 100 ks exposure time. The significance of this detection was further improved when a 1 Ms exposure time simulated observation was conducted with the HUBS satellite. The results can be seen in Table A.4 and all fitted spectra are in Figures B.7, B.8 and B.9.

In the last region, where the simulations were conducted, the average number density of particles was  $(7.3 \pm 2.1) \times 10^{-5} \text{ cm}^{-3}$ . In our dataset, this region represents a WHIM-like filament – the hidden baryons of the cosmic

## 5. CONCLUSION

---

web. We conducted 100 ks simulated observations with all the available instruments and a 1 Ms exposure time observation with the HUBS and LEM satellites. As for the future of mapping the baryons of the universe, the results (in Table 4.1) were very promising. The NewAthena X-IFU instrument did unfortunately not succeed in the WHIM component distinction, with the normalisation of this component capped at the upper limit of  $< 1.4 \times 10^{-6}$ . However, both HUBS and LEM IFU resolved the WHIM component from the background components in their spectra. The normalisation of the WHIM component for HUBS was (using  $1\sigma$  levels)  $1.4_{-1.0}^{+1.1} \times 10^{-5}$ , but simulating a 1 Ms observation, the uncertainty lowered to  $1.4_{-0.7}^{+0.8} \times 10^{-5}$ . Similarly, the LEM IFU 100 ks observation yielded the WHIM component normalisation of  $3.1_{-2.7}^{+8.3} \times 10^{-5}$ , but simulating a 1 Ms spectrum significantly improved the fit result as  $1.66_{-0.11}^{+0.17} \times 10^{-4}$ . All the fitted spectra can be seen in Figures 4.8, 4.9 and 4.10.

These results are truly fascinating. Especially from the WHIM region fitted spectra, we can see, that the abilities of future X-ray missions are far beyond the abilities of missions of today. Implementing the TES-based microcalorimeter arrays, the satellites such as NewAthena, HUBS and LEM will eventually probe the universe further away from the brightest and most massive clusters and halos. We can expect them to directly discover the hidden baryons in the filaments of the cosmic web.



## Bibliography

1. *A Chandra Pocket Guide* [online]. The Chandra X-Ray Center, 2023 [visited on 2024-04-19]. Available from: [https://cxc.harvard.edu/cdo/pocket\\_guide.pdf](https://cxc.harvard.edu/cdo/pocket_guide.pdf).
2. *An X-ray Data Primer: What I Wish I Knew when Starting X-Ray Astronomy* [online]. The Chandra X-Ray Center, 2023 [visited on 2024-04-19]. Available from: [https://cxc.cfa.harvard.edu/cdo/xray\\_primer.pdf](https://cxc.cfa.harvard.edu/cdo/xray_primer.pdf).
3. ARNAUD, K. A. XSPEC: The First Ten Years. *Astronomical Data Analysis Software and Systems V* [online]. 1996, vol. 101 [visited on 2024-05-06]. Available from: <https://ui.adsabs.harvard.edu/abs/1996ASPC..101...17A>.
4. *Athena mission webpage* [online]. Athena Community Office [visited on 2024-04-19]. Available from: <https://www.the-athena-x-ray-observatory.eu/en>.
5. BALUCINSKA-CHURCH, M. et al. Photoelectric Absorption Cross Sections with Variable Abundances. *Astrophysical Journal* [online]. 1992, vol. 400, no. 699 [visited on 2024-05-11]. Available from: <https://ui.adsabs.harvard.edu/abs/1992ApJ...400..699B/abstract>.
6. BAMBI, C.; JIANG, J. (editors). *High-Resolution X-ray Spectroscopy: Instrumentation, Data Analysis, and Science*. 1st ed. 2023.
7. BREGMAN, J. et al. Scientific objectives of the Hot Universe Baryon Surveyor (HUBS) mission. *Science China Physics, Mechanics & Astronomy* [online]. 2023, vol. 66, no. 299513 [visited on 2024-04-19]. Available from: <https://doi.org/10.1007/s11433-023-2149-y>.
8. CASH, W. Parameter estimation in astronomy through application of the likelihood ratio. *Astrophysical Journal* [online]. 1979, vol. 228 [visited on 2024-05-06]. Available from: <https://ui.adsabs.harvard.edu/abs/1979ApJ...228..939C>.
9. CEN, R.; OSTRICKER, J. P. Where Are the Baryons? *Astrophysical Journal* [online]. 1999, vol. 514, no. 1 [visited on 2024-05-08]. Available from: <https://dx.doi.org/10.1086/306949>.
10. *Chandra X-ray Observatory* [online]. The Chandra X-Ray Center [visited on 2024-04-19]. Available from: <https://chandra.harvard.edu/>.

## BIBLIOGRAPHY

---

11. CHARPAK, G.; SAULI, F. High-resolution Electronic Particle Detectors. *European organization for nuclear research* [online]. 1984 [visited on 2024-04-19]. Available from: <https://cds.cern.ch/record/150959/files/CM-P00071036.pdf>.
12. CUI, W. et al. HUBS: Hot Universe Baryon Surveyor. *Journal of Low Temperature Physics* [online]. 2020, vol. 199 [visited on 2024-04-19]. Available from: <https://doi.org/10.1007/s10909-019-02279-3>.
13. *European Space Agency Science Portal* [online]. ESA [visited on 2024-03-02]. Available from: <https://sci.esa.int/web/>.
14. *High Energy Astrophysics Science Archive Research Center* [online]. NASA [visited on 2024-04-19]. Available from: <https://heasarc.gsfc.nasa.gov/>.
15. HITOMI COLLABORATION. The quiescent intracluster medium in the core of the Perseus cluster. *Nature* [online]. 2016, vol. 535 [visited on 2024-04-19]. ISSN 1476-4687. Available from: <https://doi.org/10.1038/nature18627>.
16. *HUBS mission webpage* [online]. The HUBS Collaboration [visited on 2024-04-19]. Available from: <http://hubs.phys.tsinghua.edu.cn/en/>.
17. KAASTRA, J. S. et al. Thermal Radiation Processes. *Space Science Reviews* [online]. 2008, vol. 134 [visited on 2024-05-08]. Available from: <https://doi.org/10.1007/s11214-008-9310-y>.
18. KITAYAMA, T. et al. ASTRO-H White Paper - Clusters of Galaxies and Related Science. *arXiv e-prints* [online]. 2014 [visited on 2024-04-19]. Available from: <https://doi.org/10.48550/arXiv.1412.1176>.
19. KOVÁCS, O. E. et al. Detection of the Missing Baryons toward the Sightline of H1821+643. *Astrophysical Journal* [online]. 2019, vol. 872, no. 83 [visited on 2024-05-10]. Available from: <https://dx.doi.org/10.3847/1538-4357/aaef78>.
20. KRAFT, R. et al. Line Emission Mapper (LEM): Probing the physics of cosmic ecosystems. *arXiv e-prints* [online]. 2022 [visited on 2024-04-19]. Available from: <https://doi.org/10.48550/arXiv.2211.09827>.
21. LODDERS, K. et al. Abundances of the Elements in the Solar System. *Solar System, Landolt-Börnstein – Group VI Astronomy and Astrophysics* [online]. 2009, vol. 4B [visited on 2024-05-11]. Available from: [https://materials.springer.com/lb/docs/sm\\_lbs\\_978-3-540-88055-4\\_34](https://materials.springer.com/lb/docs/sm_lbs_978-3-540-88055-4_34).

22. MCCAMMON, D. et al. A High Spectral Resolution Observation of the Soft X-Ray Diffuse Background with Thermal Detectors. *Astrophysical Journal* [online]. 2002, vol. 576, no. 188 [visited on 2024-05-08]. Available from: <https://doi.org/10.1086/341727>.
23. MILLER, E. D. et al. Suzaku Observations of the North Polar Spur: Evidence for Nitrogen Enhancement. *Publications of the Astronomical Society of Japan* [online]. 2008, vol. 60, no. 1 [visited on 2024-05-10]. Available from: <https://doi.org/10.1093/pasj/60.sp1.S95>.
24. MOLNAR, S. M. et al. Accretion Shocks in Clusters of Galaxies and their SZ Signature from Cosmological Simulations. *Astrophysical Journal* [online]. 2009, vol. 696, no. 1640 [visited on 2024-05-09]. Available from: <https://doi.org/10.1088/0004-637X/696/2/1640>.
25. *NASA Science* [online]. NASA [visited on 2024-04-19]. Available from: <https://science.nasa.gov/>.
26. NELSON, D. et al. Introducing the TNG-Cluster Simulation: overview and physical properties of the gaseous intracluster medium. *Astronomy & Astrophysics* [online]. 2024 [visited on 2024-05-08]. Available from: <https://doi.org/10.48550/arXiv.2311.06338>.
27. NELSON, D. et al. The IllustrisTNG Simulations: Public Data Release. *Computational Astrophysics and Cosmology* [online]. 2019, vol. 6, no. 1 [visited on 2024-04-19]. Available from: <https://doi.org/10.48550/arXiv.1812.05609>.
28. NICASTRO, F. et al. Observations of the missing baryons in the warm-hot intergalactic medium. *Nature* [online]. 2018, vol. 558 [visited on 2024-05-09]. Available from: <https://doi.org/10.1038/s41586-018-0204-1>.
29. *pyXSIM Documentation* [online]. Zuhone, J. [visited on 2024-04-19]. Available from: <https://hea-www.cfa.harvard.edu/~jzuhone/pyxsim/>.
30. SCHNEIDER, P. *Extragalactic Astronomy and Cosmology: An introduction*. 2nd ed. 2015.
31. *Science with the Athena X-ray Integral Field Unit, X-IFU Preliminary Requirements Review* [online]. D. Barret and the X-IFU science advisory team, 2019 [visited on 2024-04-19]. Available from: [https://x-ifu.irap.omp.eu/wp-content/uploads/2021/04/XIFU-SN-XI-09012019-IRAP-compressed\\_2.pdf](https://x-ifu.irap.omp.eu/wp-content/uploads/2021/04/XIFU-SN-XI-09012019-IRAP-compressed_2.pdf).

## BIBLIOGRAPHY

---

32. *Science with the X-ray Imaging and Spectroscopy Mission (XRISM)* [online]. XRISM Science Team, 2022 [visited on 2024-05-08]. Available from: <https://www.cosparathens2022.org/>.
33. SIMIONESCU, A. et al. Voyage through the hidden physics of the cosmic web. *Experimental Astronomy* [online]. 2021, vol. 51 [visited on 2024-04-19]. Available from: <https://doi.org/10.1007/s10686-021-09720-0>.
34. *SOXS: Simulated Observations of X-ray Sources* [online]. John ZuHone, 2024 [visited on 2024-04-19]. Available from: <https://hea-www.cfa.harvard.edu/soxs/index.html>.
35. ŠTOFANOVÁ, L. et al. Galaxy cluster photons alter the ionization state of the nearby warm-hot intergalactic medium. *Monthly Notices of the Royal Astronomical Society* [online]. 2022, vol. 515 [visited on 2024-04-19]. ISSN 1365-2966. Available from: <https://doi.org/10.1093/mnras/stac1854>.
36. SVAČINKOVÁ, K. *Characterising the unresolved emission in the Chandra Deep Field-South*. 2023. MA thesis. Masaryk University.
37. TAKAHASHI, T. et al. The ASTRO-H X-ray Astronomy Satellite. *Space Telescopes and Instrumentation 2014: Ultraviolet to Gamma Ray* [online]. 2014, vol. 9144 [visited on 2024-04-19]. Available from: <https://doi.org/10.1117/12.2055681>.
38. *The TNG Project* [online]. TNG Collaboration [visited on 2024-04-19]. Available from: <https://www.tng-project.org/>.
39. *The yt Project* [online]. The yt Community [visited on 2024-04-19]. Available from: <https://yt-project.org/>.
40. VOGES, W. et al. The ROSAT all-sky survey bright source catalogue. *Astronomy & Astrophysics* [online]. 1999, vol. 349, no. 389 [visited on 2024-05-08]. Available from: <https://doi.org/10.48550/arXiv.astro-ph/9909315>.
41. WERNER, N.; MERNIER, F. Hot atmospheres of galaxies, groups, and clusters of galaxies. *Reviews in Frontiers of Modern Astrophysics* [online]. 2020 [visited on 2024-04-19]. Available from: [https://doi.org/10.1007/978-3-030-38509-5\\_10](https://doi.org/10.1007/978-3-030-38509-5_10).
42. WERNER, N. et al. Hot Atmospheres, Cold Gas, AGN Feedback and the Evolution of Early Type Galaxies: A Topical Perspective. *Space Science Reviews* [online]. 2019, vol. 215, no. 1 [visited on 2024-05-08]. Available from: <https://doi.org/10.1007/s11214-018-0571-9>.

43. WERNER, N. et al. Detection of hot gas in the filament connecting the clusters of galaxies Abell 222 and Abell 223. *Astronomy & Astrophysics* [online]. 2008, vol. 482, no. 3 [visited on 2024-04-19]. ISSN 0004-6361. Available from: <https://doi.org/10.1051/0004-6361:200809599>.
44. *XMM-Newton Users Handbook* [online]. XMM-Newton Community Support Team, 2023 [visited on 2024-03-02]. Available from: [http://xmm-tools.cosmos.esa.int/external/xmm\\_user\\_support/documentation/uhb/XMM\\_UHB.pdf](http://xmm-tools.cosmos.esa.int/external/xmm_user_support/documentation/uhb/XMM_UHB.pdf).
45. *XRISM Quick Reference* [online]. XRISM Science Team, 2022 [visited on 2024-05-08]. Available from: [https://xrism.isas.jaxa.jp/research/analysis/manuals/xrqr\\_v2.1.pdf](https://xrism.isas.jaxa.jp/research/analysis/manuals/xrqr_v2.1.pdf).
46. ZHANG, C. et al. Mapping the Intracluster Medium in the Era of High-resolution X-ray Spectroscopy. *Monthly Notices of the Royal Astronomical Society* [online]. 2023, vol. 1, no. 24 [visited on 2024-04-19]. Available from: <https://doi.org/10.48550/arXiv.2310.02225>.
47. ZINGLER, E. et al. Ejective and preventative: the IllustrisTNG black hole feedback and its effects on the thermodynamics of the gas within and around galaxies. *Monthly Notices of the Royal Astronomical Society* [online]. 2020, vol. 499 [visited on 2024-05-08]. ISSN 1365-2966. Available from: <https://doi.org/10.1093/mnras/staa2607>.
48. ZUHONE, J. A.; HALLMAN, E. J. pyXSIM: Synthetic X-ray observations generator. *Astrophysics Source Code Library* [online]. 2016 [visited on 2024-05-06]. Available from: <https://ui.adsabs.harvard.edu/abs/2016ascl.soft08002Z>.
49. ZUHONE, J. A. et al. SOXS: Simulated Observations of X-ray Sources. *Astrophysics Source Code Library* [online]. 2023 [visited on 2024-05-06]. Available from: <https://ui.adsabs.harvard.edu/abs/2023ascl.soft01024Z>.



## **A Results: tables for remaining regions**

**Table A.1: Resulting fitted parameters of the halo center.**

| Instrument        | Fit method | FITTING RESULTS :: HALO CENTER |  |                         |              | Abundance                                | Statistic<br>Cstat/DOF              |
|-------------------|------------|--------------------------------|--|-------------------------|--------------|--|-------------------------------------|
|                   |            | <i>apec</i>                    | Background components<br><i>phabs*apec</i> | <i>powerlaw</i>         | Photon index |  |                                     |
| Chandra           | bkg+apec   | -                              | -  | $< 7.31 \times 10^{-6}$ | 1.5          | $7.34^{+0.04}_{-0.03} \times 10^{-2}$    | 1.7 ± 0.2<br>1184 / 437             |
| XRISM             | bkg+apec   | -                              | -  | $< 1.41 \times 10^{-3}$ | 1.5          | $(1.45 \pm 0.02) \times 10^{-2}$         | $0.237 \pm 0.013$<br>16455 / 16992  |
| NewAthena         | bkg+apec   | $(2.0 \pm 0.7) \times 10^{-5}$ | $(1.2 \pm 0.2) \times 10^{-5}$             | $< 5.81 \times 10^{-5}$ | 1.5          | $1.186^{+0.008}_{-0.019} \times 10^{-2}$ | $0.210 \pm 0.005$<br>19879 / 21842  |
| HUBS              | bkg+apec   | $(6.1 \pm 1.3) \times 10^{-5}$ | $(3.4 \pm 0.6) \times 10^{-5}$             | $< 1.08 \times 10^{-4}$ | 1.5          | $2.513^{+0.010}_{-0.047} \times 10^{-2}$ | $0.121 \pm 0.010$<br>20023 / 17992  |
| LEM               | bkg+apec   | $(8.0 \pm 0.8) \times 10^{-5}$ | $(3.4 \pm 0.4) \times 10^{-5}$             | $< 4.15 \times 10^{-5}$ | 1.5          | $3.316^{+0.018}_{-0.006} \times 10^{-2}$ | $0.148 \pm 0.005$<br>9506 / 17191   |
| Region parameters |            | -                              | -  | -                       | -            | $4.2 \pm 0.4$                            | $(3.0 \pm 0.9) \times 10^{-1}$<br>- |

**Table A.2: Resulting fitted parameters of the halo  $r_{500}$  region.**

| Instrument        | Fit method | FITTING RESULTS :: HALO $r_{500}$ |  |                                    |              | Abundance                             | Statistic<br>Cstat/DOF                                 |
|-------------------|------------|-----------------------------------|--|------------------------------------|--------------|---------------------------------------|--|
|                   |            | <i>apec</i>                       | Background components<br><i>phabs*apec</i> | <i>powerlaw</i>                    | Photon index |                                       |  |
| XRISM             | bkg+apec   | -                                 | -  | $< 8.22 \times 10^{-4}$            | 1.5          | $2.1^{+1.4}_{-1.2} \times 10^{-2}$    | $0.11^{+0.07}_{-0.05} \times 10^{-2}$<br>10656 / 16993 |
| NewAthena         | bkg+apec   | $(3.26 \pm 0.08) \times 10^{-5}$  | $(1.42 \pm 0.03) \times 10^{-5}$           | $(1.91 \pm 0.10) \times 10^{-5}$   | 1.5          | $(1.20 \pm 0.04) \times 10^{-4}$      | $(3.4 \pm 0.5) \times 10^{-2}$<br>14262 / 21837        |
| HUBS              | bkg+apec   | $(5.9 \pm 0.2) \times 10^{-5}$    | $(2.52 \pm 0.08) \times 10^{-5}$           | $< 1.27 \times 10^{-5}$            | 1.5          | $3.80^{+0.05}_{-0.53} \times 10^{-4}$ | $3.5^{+0.8}_{-0.7} \times 10^{-2}$<br>17603 / 17993    |
| LEM               | bkg+apec   | $(8.24 \pm 0.10) \times 10^{-5}$  | $(3.56 \pm 0.05) \times 10^{-5}$           | $4.1^{+1.5}_{-1.7} \times 10^{-5}$ | 1.5          | $3.9^{+0.7}_{-0.6} \times 10^{-4}$    | $4.8^{+0.7}_{-0.6} \times 10^{-2}$<br>7831 / 1793      |
| Region parameters |            | -                                 | -  | -                                  | -            | $2.6 \pm 0.5$                         | $(1.7 \pm 0.3) \times 10^{-1}$<br>-                    |



**Table A.3:** Resulting fitted parameters of the halo  $r_{200}$  region.

| FITTING RESULTS :: HALO $r_{200}$ |            |                                       |                                  |                                     |                        |                     |                                    |             |                        |
|-----------------------------------|------------|---------------------------------------|----------------------------------|-------------------------------------|------------------------|---------------------|------------------------------------|-------------|------------------------|
| Instrument                        | Fit method | Background components                 |                                  |                                     | Photon index           | Gas component       |                                    | Abundance   | Statistic<br>Cstat/DOF |
|                                   |            | <i>apec</i>                           | <i>phabs*apec</i>                | <i>powerlaw</i>                     |                        | Temperature (keV)   | Normalisation                      |             |                        |
| XRISM                             | bkg+apec   | -                                     | -                                | $5.2^{+2.5}_{-1.2} \times 10^{-4}$  | $1.4^{+0.2}_{-0.1}$    | $6.6^{+4.1}_{-4.0}$ | $1.2 \times 10^{-1}$               | 5938/16992  |                        |
| NewAthena                         | bkg+apec   | $(3.36 \pm 0.07) \times 10^{-5}$      | $(1.39 \pm 0.02) \times 10^{-5}$ | $7.4^{+1.1}_{-1.4} \times 10^{-6}$  | $1.57^{+0.08}_{-0.10}$ | $2.0^{+0.9}_{-0.4}$ | $5.1^{+6.8}_{-2.6} \times 10^{-2}$ | 10506/21836 |                        |
| HUBS                              | bkg+apec   | $(6.01 \pm 0.16) \times 10^{-5}$      | $(2.73 \pm 0.08) \times 10^{-5}$ | $7.9^{+14.3}_{-4.2} \times 10^{-6}$ | $0.7 \pm 1.0$          | $1.2 \pm 0.2$       | $< 7.66 \times 10^{-3}$            | 12827/17992 |                        |
| LEM                               | bkg+apec   | $8.22^{+0.11}_{-0.12} \times 10^{-5}$ | $(3.51 \pm 0.05) \times 10^{-5}$ | $(2.5 \pm 0.7) \times 10^{-5}$      | 1.5                    | $2.0^{+0.3}_{-0.4}$ | $1.3 \pm 0.7 \times 10^{-2}$       | 7436/7193   |                        |
| Region parameters                 |            | -                                     | -                                | -                                   | -                      | $2.4 \pm 0.2$       | $(1.2 \pm 0.2) \times 10^{-1}$     | -           |                        |

**Table A.4:** Resulting fitted parameters of the region beyond the halo beyond  $r_{200}$  region.

| FITTING RESULTS :: HALO BEYOND $r_{200}$ |            |                                  |                                    |  |                           |                      |                                |             |                        |
|--|------------|----------------------------------|------------------------------------|--|---------------------------|----------------------|--------------------------------|-------------|------------------------|
| Instrument                               | Fit method | Background components            |                                    |  | Photon index              | Gas component        |                                | Abundance   | Statistic<br>Cstat/DOF |
|  |            | <i>apec</i>                      | <i>phabs*apec</i>                  | <i>powerlaw</i>                        |                           | Temperature (keV)    | Normalisation                  |             |                        |
| XRISM                                    | bkg+apec   | -                                | -                                  | $(1.76 \pm 0.08) \times 10^{-3}$       | $1.9^{+0.5}_{-0.4}$       | $10.0^{+8.5}_{-3.2}$ | $1.0 \times 10^{-1}$           | 1008/16993  |                        |
| NewAthena                                | bkg+apec   | $(3.26 \pm 0.07) \times 10^{-5}$ | $(1.42 \pm 0.02) \times 10^{-5}$   | $8.5^{+0.7}_{-1.1} \times 10^{-6}$     | $1.69^{+0.05}_{-0.03}$    | $2.7^{+2.0}_{-0.7}$  | $1.0 \times 10^{-1}$           | 9997/21837  |                        |
|  | bkg only   | $(3.24 \pm 0.07) \times 10^{-5}$ | $(1.42 \pm 0.02) \times 10^{-5}$   | $(1.003 \pm 0.013) \times 10^{-5}$     | $1.71 \pm 0.02$           | -                    | -                              | 10006/21839 |                        |
| HUBS <sub>100ks</sub>                    | bkg+apec   | $(5.9 \pm 0.2) \times 10^{-5}$   | $(2.75 \pm 0.08) \times 10^{-5}$   | $(3.50 \pm 0.07) \times 10^{-5}$       | $1.56 \pm 0.04$           | $1.6 \pm 1.0$        | $1.0 \times 10^{-1}$           | 13614/17993 |                        |
|  | bkg only   | $(5.9 \pm 0.3) \times 10^{-5}$   | $(2.750 \pm 0.013) \times 10^{-5}$ | $(3.525 \pm 0.011) \times 10^{-5}$     | $1.58 \pm 0.07$           | -                    | -                              | 13623/17995 |                        |
| HUBS <sub>1Ms</sub>                      | bkg+apec   | $(5.92 \pm 0.05) \times 10^{-5}$ | $(2.67 \pm 0.03) \times 10^{-5}$   | $4.60^{+0.08}_{-0.012} \times 10^{-5}$ | $1.908^{+0.013}_{-0.011}$ | $2.3^{+0.9}_{-0.3}$  | $1.0 \times 10^{-1}$           | 19619/17993 |                        |
|  | bkg only   | $(5.92 \pm 0.05) \times 10^{-5}$ | $(2.67 \pm 0.03) \times 10^{-5}$   | $(4.77 \pm 0.02) \times 10^{-5}$       | $1.899 \pm 0.010$         | -                    | -                              | 19626/17995 |                        |
| LEM                                      | bkg+apec   | $(8.20 \pm 0.10) \times 10^{-5}$ | $(3.55 \pm 0.05) \times 10^{-5}$   | $3.5^{+0.4}_{-0.7} \times 10^{-5}$     | $1.75^{+0.08}_{-0.04}$    | $3.8^{+2.1}_{-2.0}$  | $1.0 \times 10^{-1}$           | 7238/7193   |                        |
|  | bkg only   | $(8.19 \pm 0.10) \times 10^{-5}$ | $(3.55 \pm 0.05) \times 10^{-5}$   | $(4.06 \pm 0.04) \times 10^{-5}$       | $1.72 \pm 0.02$           | -                    | -                              | 7242/7195   |                        |
| Region parameters                        |            | -                                | -                                  | -                                      | -                         | $2.1 \pm 0.3$        | $(1.0 \pm 0.3) \times 10^{-1}$ | -           |                        |



## **B Results: all remaining fitted spectra**

## B. RESULTS: ALL REMAINING FITTED SPECTRA

---

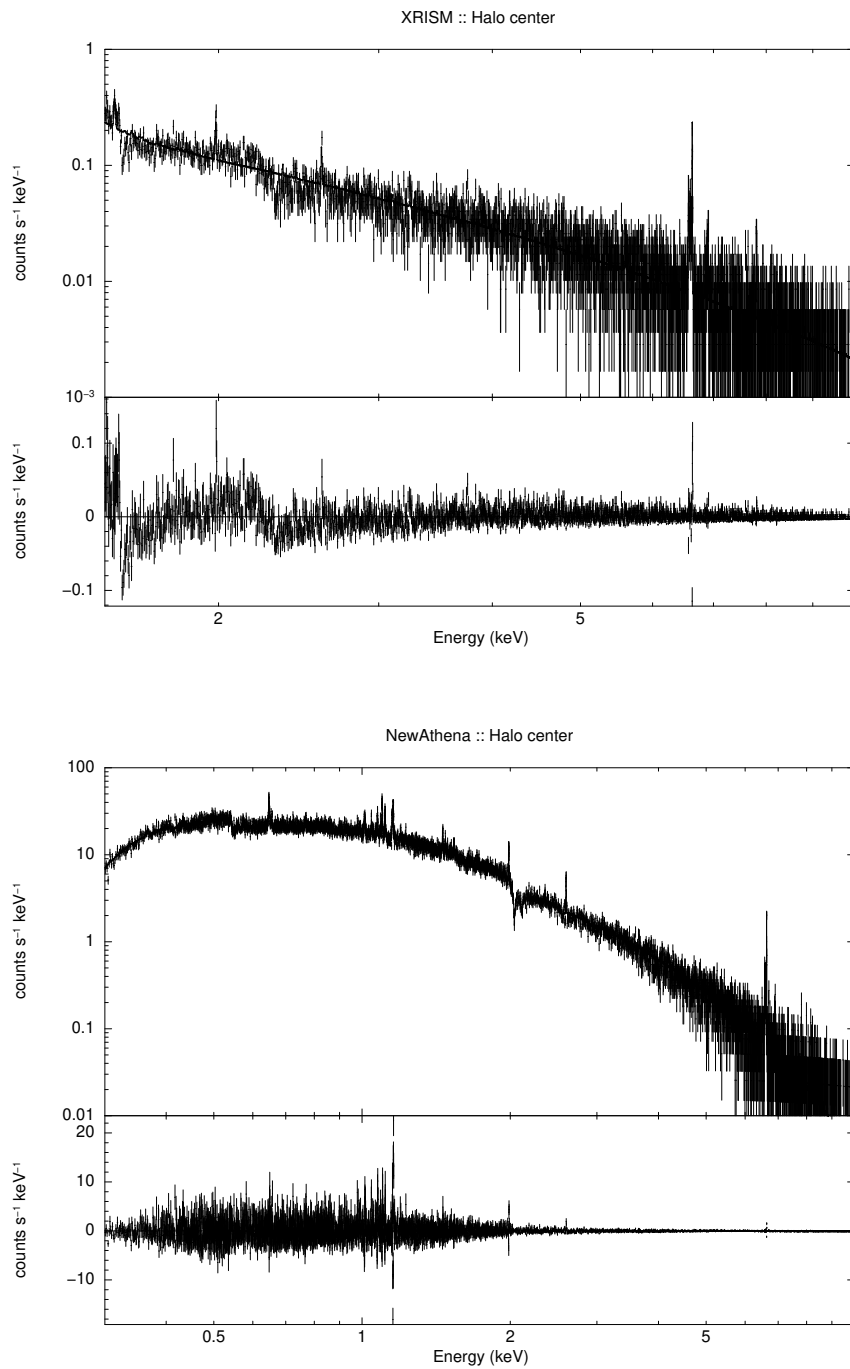


**Figure B.1:** Fitted spectra of the halo center with XRISM Resolve (top) and NewAthena X-IFU (bottom), both simulated with a 10 ks exposure time.

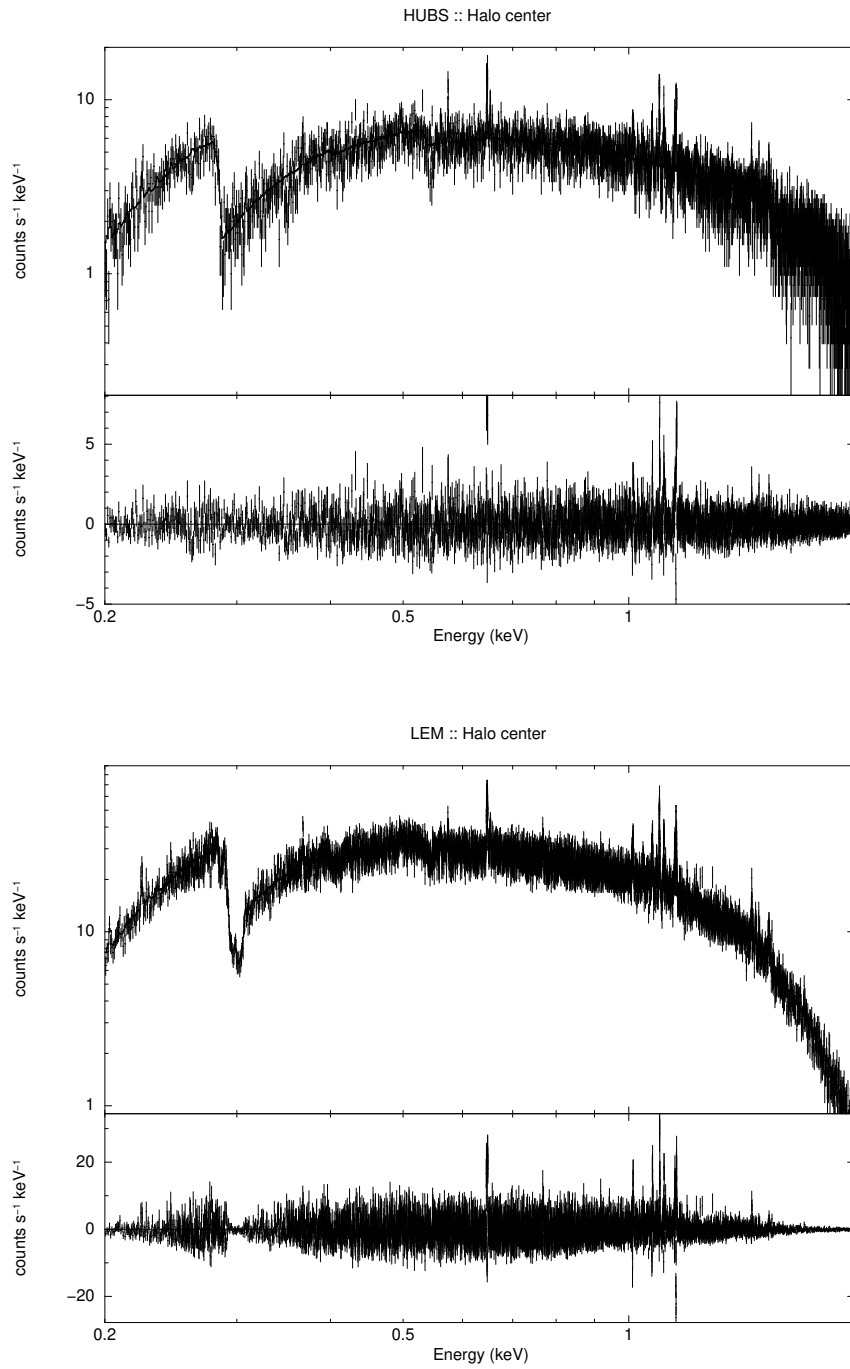


**Figure B.2:** Fitted spectra of the halo center with HUBS (top) and LEM IFU (bottom), both simulated with a 10 ks exposure time.

## B. RESULTS: ALL REMAINING FITTED SPECTRA

---

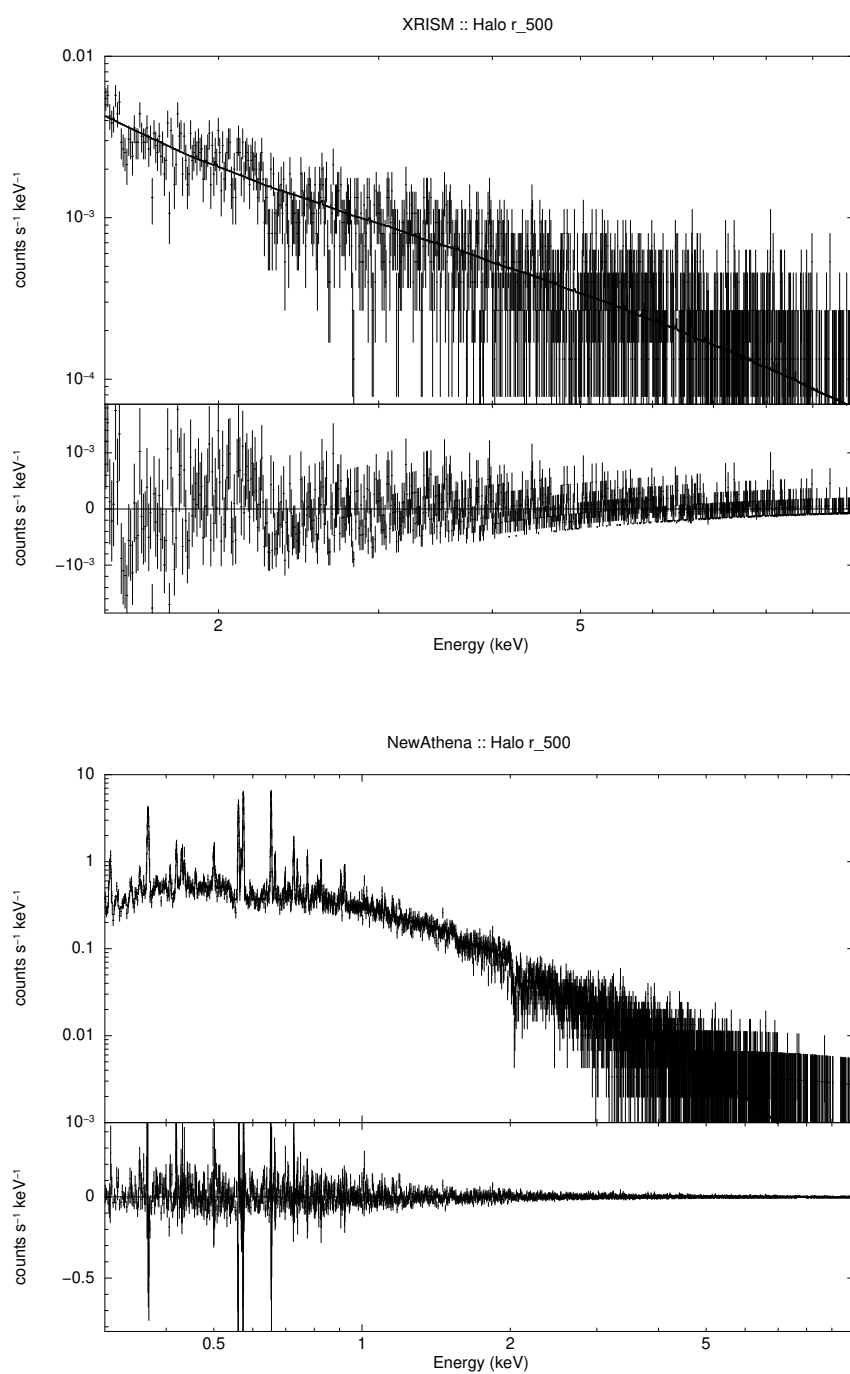


**Figure B.3:** Fitted spectra of the halo  $r_{500}$  region with XRISM Resolve (top) and NewAthena X-IFU (bottom), both simulated with a 100 ks exposure time.

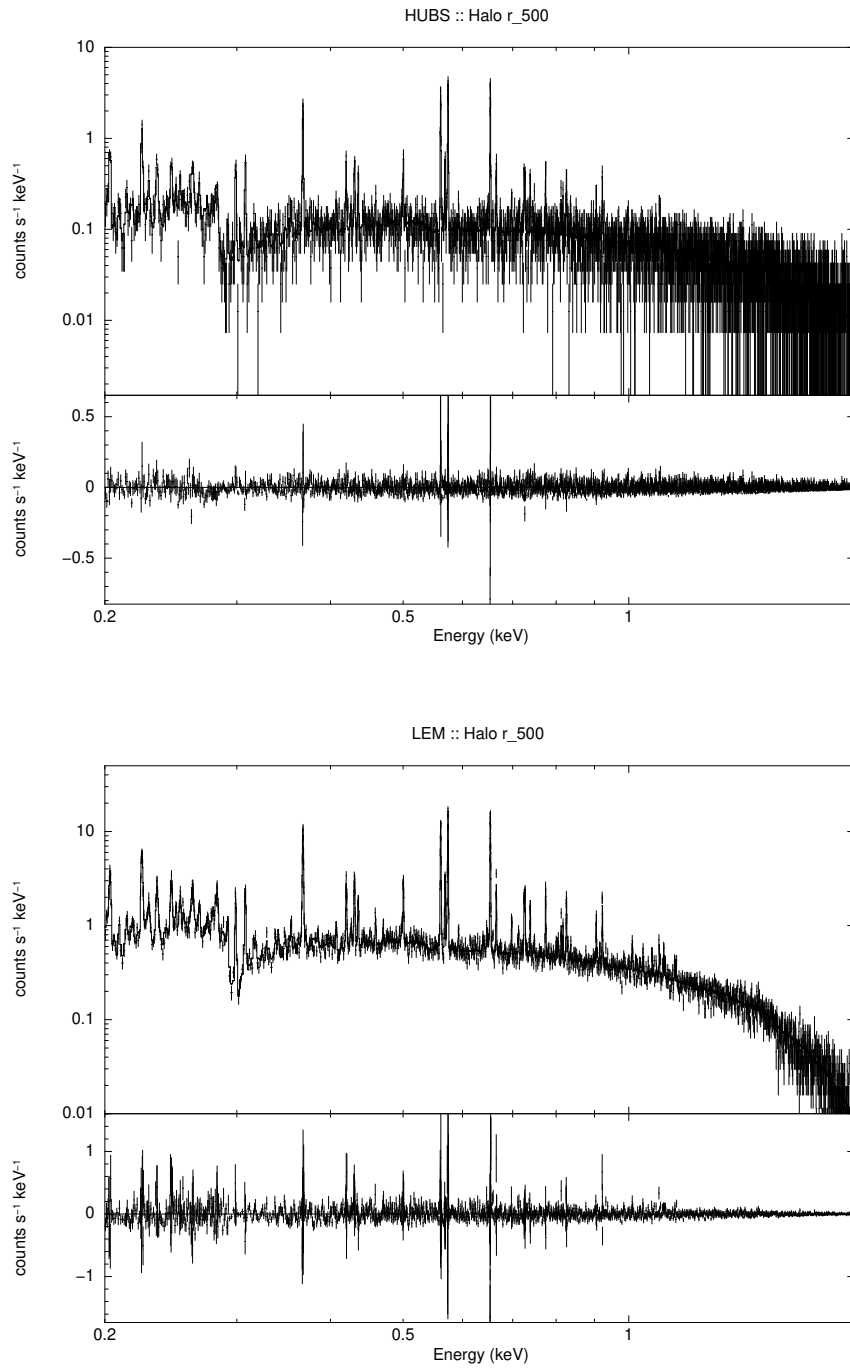


**Figure B.4:** Fitted spectra of the halo r<sub>500</sub> region with HUBS (top) and LEM IFU (bottom), both simulated with a 100 ks exposure time.

## B. RESULTS: ALL REMAINING FITTED SPECTRA

---

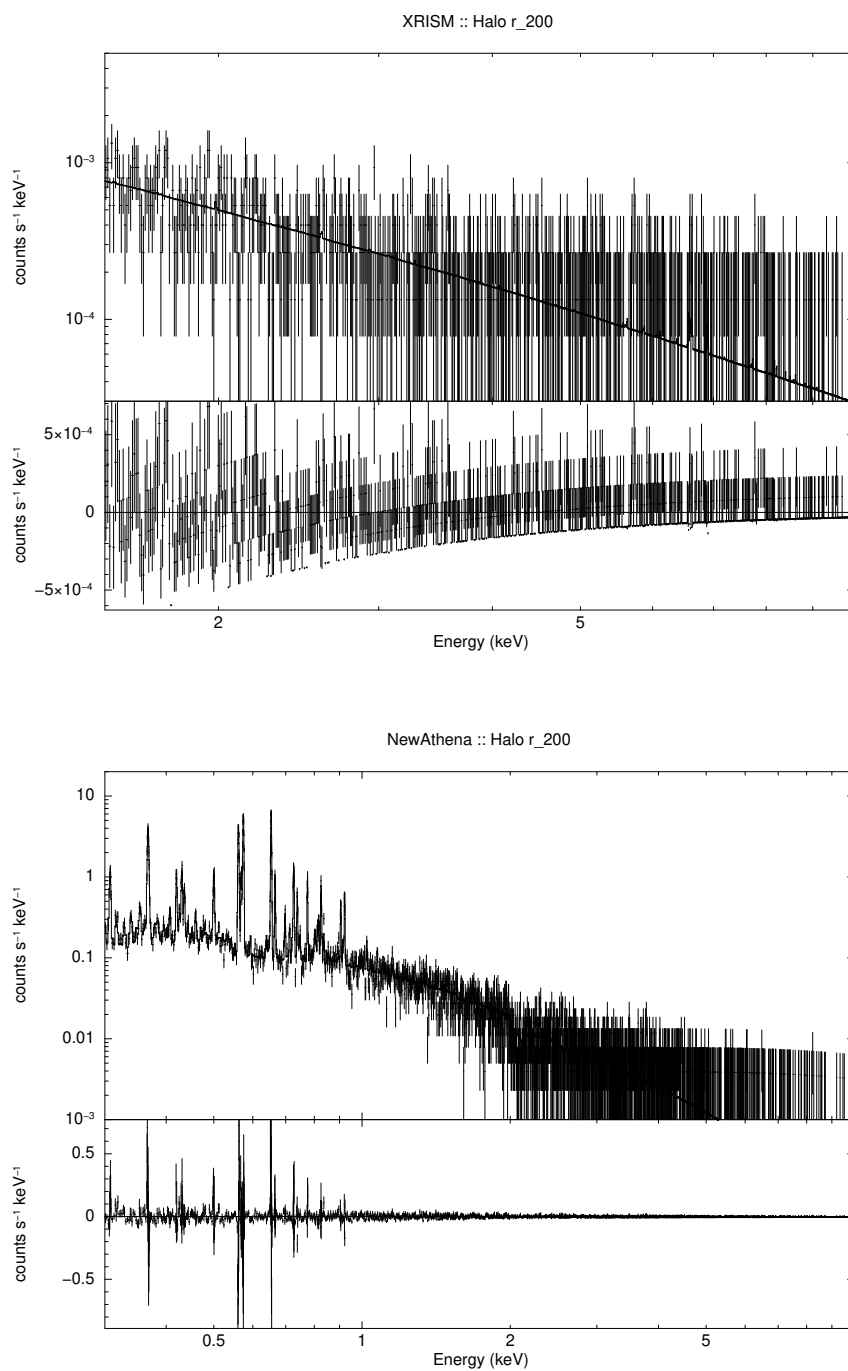


**Figure B.5:** Fitted spectra of the halo  $r_{200}$  region with XRISM Resolve (top) and NewAthena X-IFU (bottom), both simulated with a 100 ks exposure time.



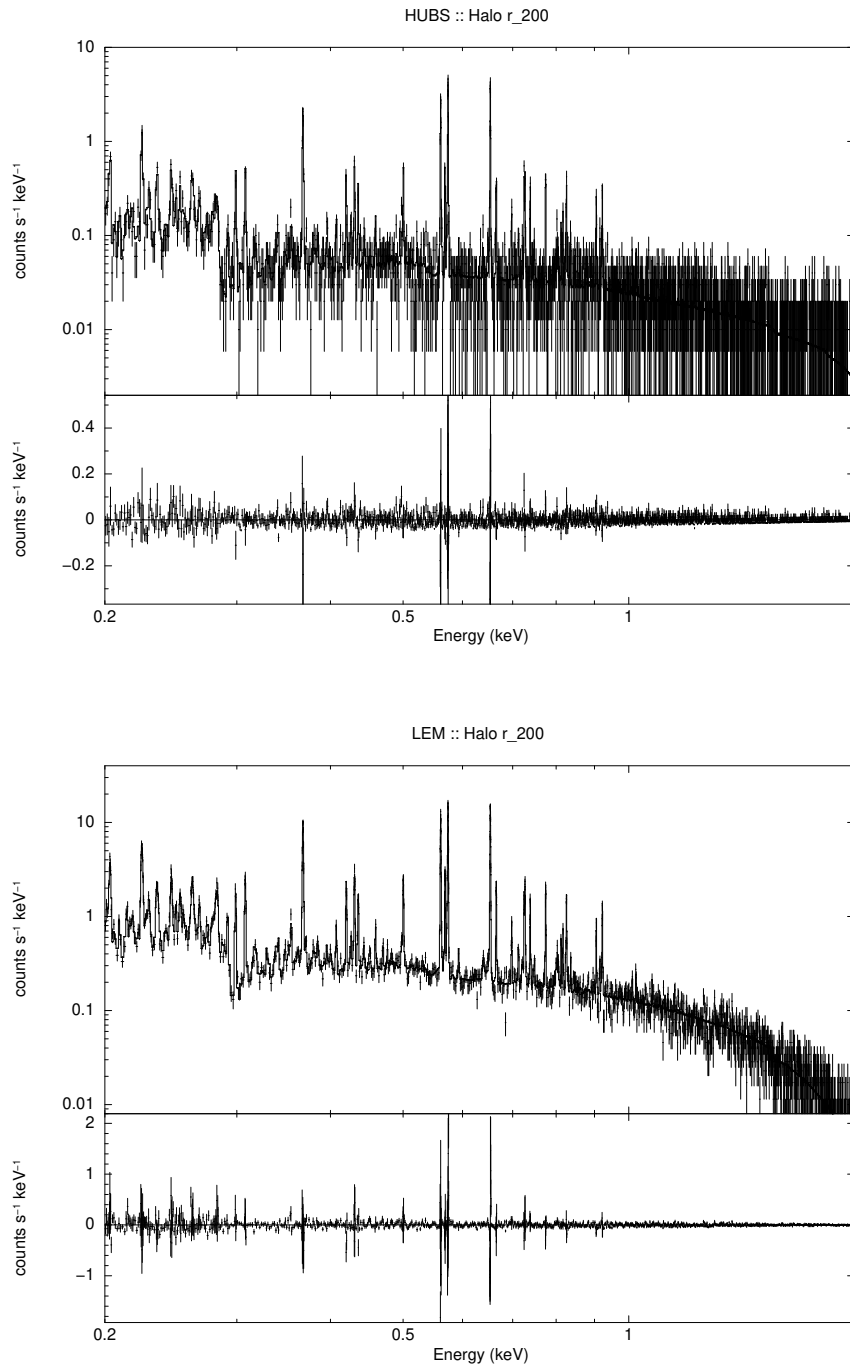


**Figure B.6:** Fitted spectra of the halo  $r_{200}$  region with HUBS (top) and LEM IFU (bottom), both simulated with a 100 ks exposure time.

## B. RESULTS: ALL REMAINING FITTED SPECTRA

---

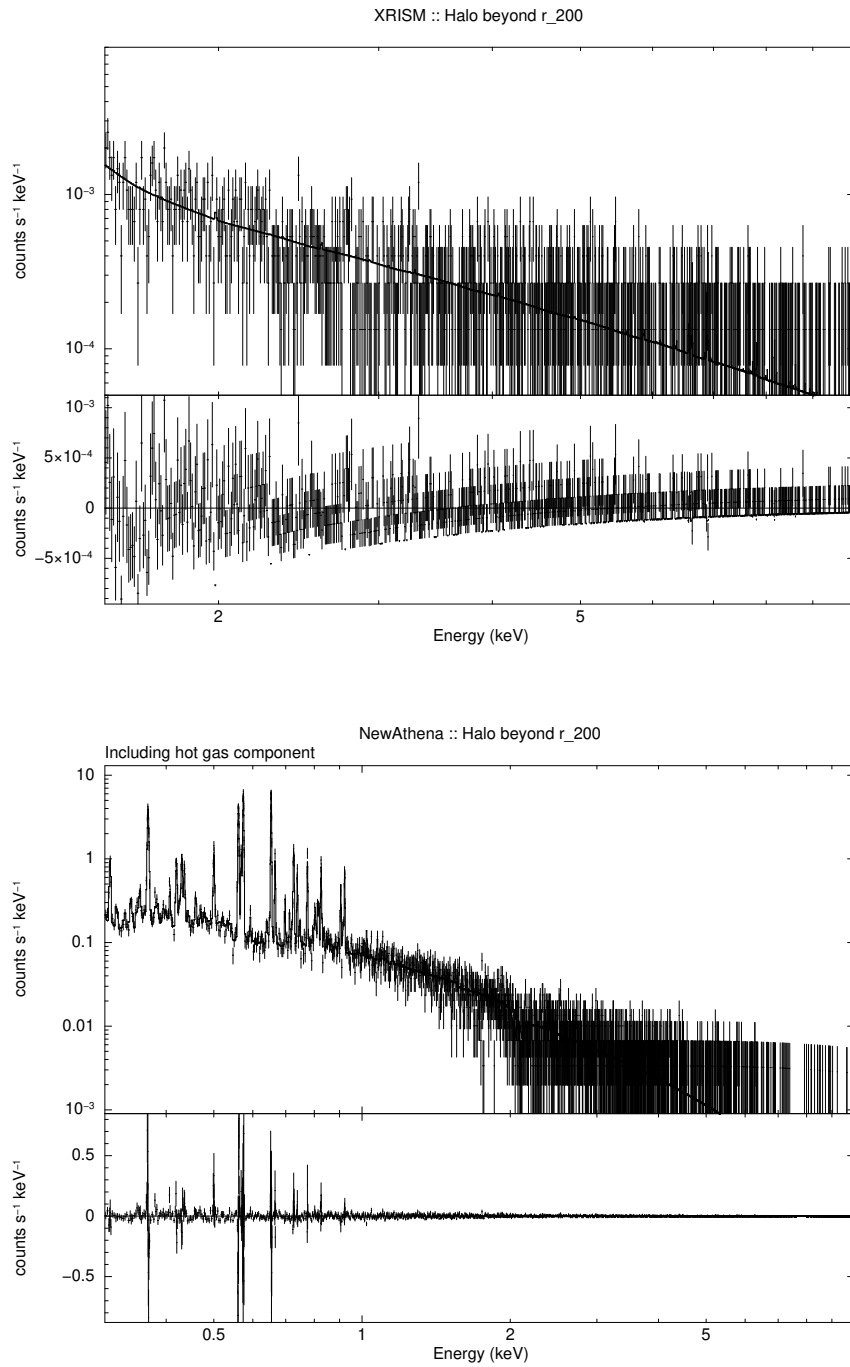


**Figure B.7:** Fitted spectra of the region beyond halo  $r_{200}$  with XRISM Resolve (top) and NewAthena X-IFU (bottom), both simulated with a 100 ks exposure time.

## B. RESULTS: ALL REMAINING FITTED SPECTRA

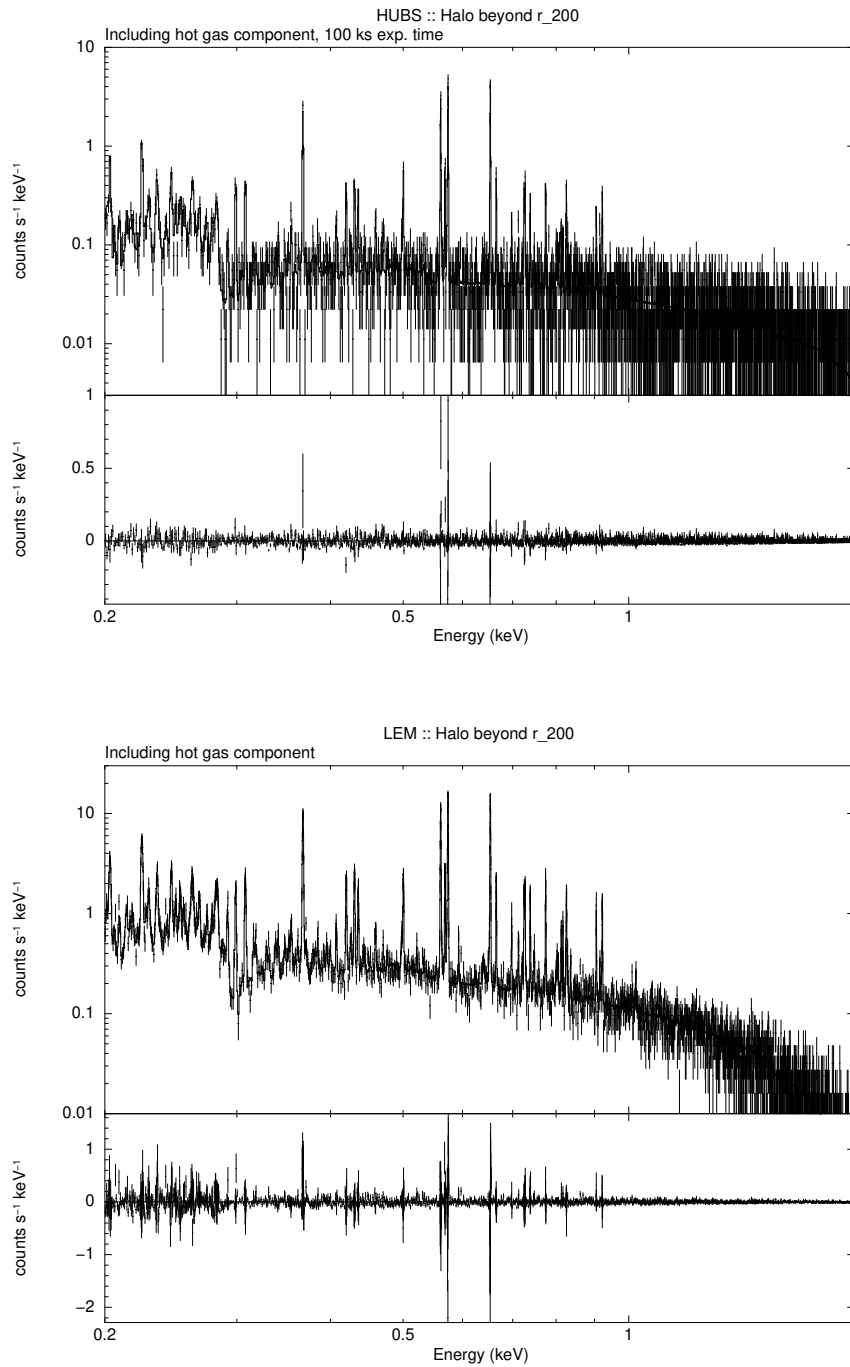


**Figure B.8:** Fitted spectra of the region beyond halo  $r_{200}$  with HUBS (top) and LEM IFU (bottom), both simulated with a 100 ks exposure time.

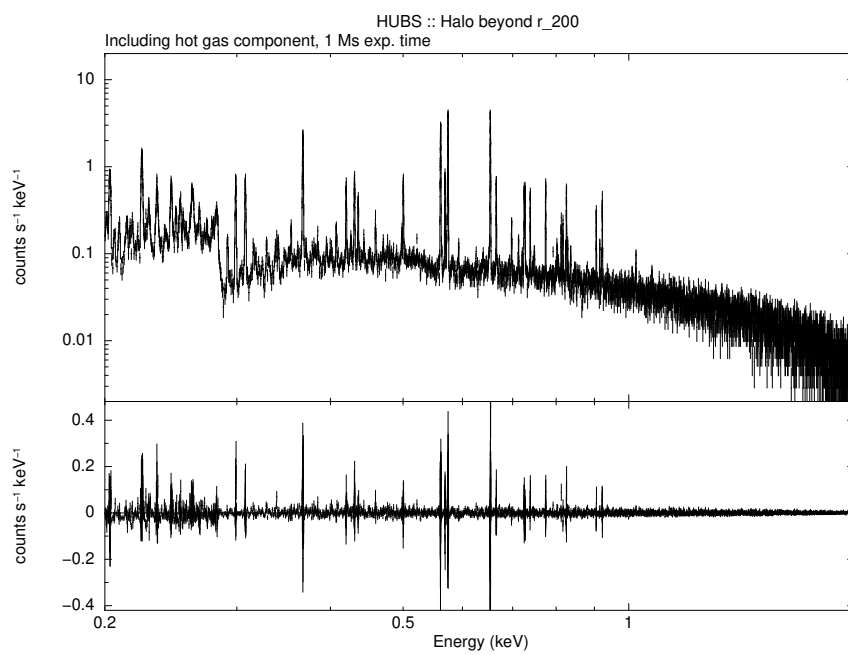


**Figure B.9:** Fitted spectrum of the region beyond halo  $r_{200}$  with HUBS, simulated with a 1 Ms exposure time.

## C Code: loading and handling of TNG data structure

The following is the code used within this thesis in order to load a TNG data structure from a downloaded file. Note that the code is structured to jupyter-notebook-like cells using the '# %%' symbols, supported by the Visual Studio Code. Most of the code structure was obtained via TNG tutorials at *The TNG Project* [38].

```
1 # %%
2 # ----- Import -----
3 from soxs.utils import soxs_cfg
4 soxs_cfg.set("soxs", "bkgnd_nH", "0.01")
5 import soxs
6 import yt
7 import pyxsim
8
9 print("pyxsim version:", pyxsim.__version__)
10 print("soxs version:", soxs.__version__)
11
12 import h5py
13 import numpy as np
14 import illustris_python as il
15
16 import os
17 from regions import RectangleSkyRegion
18 from astropy.coordinates import SkyCoord
19 import astropy.units as u
20 from astropy import wcs
21 from astropy.io import fits
22 from scipy.constants import m_p
23 # %%
24 # ----- Load data -----
25 basePath = "/space/IllustrisTNG/TNG100-3/output/"
26 snap = 99 # snap 99 = redshift 0.01
27 haloID = 0 # the most massive halo in selected snapshot
28 # %%
29 groupcat = il.groupcat.loadHalos(basePath, snap)
30 halo = il.groupcat.loadSingle(basePath, snap, haloID=haloID)
31 # %%
32 fields = ['Coordinates',
33           'GFM_CoolingRate',
34           'Density',
```

```

35         'InternalEnergy',
36         'ElectronAbundance',
37         'StarFormationRate']
38 gas = il.snapshot.loadHalo(basePath, snap, haloID, "gas")
39 header = il.groupcat.loadHeader(basePath, snap)
40
41 with h5py.File(il.snapshot.snapPath(basePath, snap), 'r') as f:
42     header_snap = dict(f['Header'].attrs)
43     # %%
44     # ----- yt settings -----
45     filename = "halo_%d.hdf5" % haloID
46     # %%
47     with h5py.File(filename, 'w') as f:
48         for key in gas.keys():
49             f['PartType0/' + key] = gas[key]
50
51         # some metadata that yt demands
52         f.create_group('Header')
53         f['Header'].attrs['NumFilesPerSnapshot'] = 1
54         f['Header'].attrs['MassTable'] = header_snap['MassTable']
55         f['Header'].attrs['BoxSize'] = header['BoxSize']
56         f['Header'].attrs['Time'] = header['Time']
57         f['Header'].attrs['NumPart_ThisFile'] =
58             → np.array([gas['count'], 0, 0, 0, 0, 0])
59
60         # Must have the next six for correct units
61         f["Header"].attrs["HubbleParam"] = header["HubbleParam"]
62         f["Header"].attrs["Omega0"] = header["Omega0"]
63         f["Header"].attrs["OmegaLambda"] = header["OmegaLambda"]
64
65         # These correspond to the values from the TNG simulations
66         f["Header"].attrs["UnitLength_in_cm"] =
67             → header_snap['UnitLength_in_cm']
68         f["Header"].attrs["UnitMass_in_g"] =
69             → header_snap['UnitMass_in_g']
70         f["Header"].attrs["UnitVelocity_in_cm_per_s"] =
71             → header_snap['UnitVelocity_in_cm_per_s']
72     # %%
73     # ----- Load yt file -----
74     ds = yt.load(filename, default_species_fields="ionized")
75     # %%
76     # ----- Add an X-ray filter -----
77     def hot_gas(pfilter, data):

```

```

74     pfilter1 = data[pfilter.filtered_type, "temperature"] >
       → 3.0e5
75     pfilter2 = data["PartType0", "StarFormationRate"] == 0.0
76     pfilter3 = data["PartType0", "GFM_CoolingRate"] < 0.0
77     return (pfilter1 & pfilter2) & pfilter3
78
79 yt.add_particle_filter("hot_gas",
80                       function=hot_gas,
81                       filtered_type='gas',
82                       requires=["temperature", "density"])
83 # %%
84 ds.add_particle_filter("hot_gas")
85 # %%
86 # ----- Projection and visualisation -----
87 c = ds.arr([halo["GroupPos"][0],
88            halo["GroupPos"][1],
89            halo["GroupPos"][2]],
90            "code_length")
91 # %%
92 # Define shift values
93 dx, dy, dz = 0.0, 0.0, 0.0 # halo center
94 # dx, dy, dz = 0.0, 0.0, -2000.0 # halo 0 filament
95 # dx, dy, dz = 0.0, 0.0, 600.0 # halo 0 beyond r200
96 # dx, dy, dz = 0.0, 0.0, 470.0 # halo 0 r200
97 # dx, dy, dz = 0.0, 0.0, 295.0 # halo 0 r500
98
99 # Shift the center of projection
100 c_shifted = ds.arr([halo["GroupPos"][0] + dx,
101                   halo["GroupPos"][1] + dy,
102                   halo["GroupPos"][2] + dz],
103                   "code_length")
104 # %%
105 # Gas density projection
106 sphere_center = c
107 r0_pt = ds.quan(10, 'kpc')
108 r200_sp = ds.quan(696.5179446533203, 'kpc')
109 r500_sp = ds.quan(436.4346303222656, 'kpc')
110 prj = yt.ProjectionPlot(ds,
111                          "x",
112                          ("gas", "density"),
113                          width=(7, "Mpc"),
114                          center=c_shifted)
115 prj.annotate_sphere(c_shifted,

```

```

116         radius=r0_pt,
117         circle_args={'color':'black',
118                     'linestyle':'solid'})
119 prj.annotate_sphere(sphere_center,
120                    radius=r200_sp,
121                    circle_args={'color':'red',
122                                'linestyle':'dashed'})
123 prj.annotate_sphere(sphere_center,
124                    radius=r500_sp,
125                    circle_args={'color':'black',
126                                'linestyle':'dashed'})
127 prj.set_zlim(("gas","density"), 1.0e-8, 1.0e-2)
128 prj.show()
129 # %%
130 # Gas temperature slice
131 sphere_center = c
132 r0_pt = ds.quan(10, 'kpc')
133 r200_sp = ds.quan(696.517944653320, 'kpc')
134 r500_sp = ds.quan(436.4346303222656, 'kpc')
135 slc = yt.SlicePlot(ds,
136                   "x",
137                   ("gas","temperature"),
138                   width=(7, "Mpc"),
139                   center=c_shifted)
140 slc.annotate_sphere(c_shifted,
141                   radius=r0_pt,
142                   circle_args={'color':'black',
143                               'linestyle':'solid'})
144 slc.annotate_sphere(sphere_center,
145                   radius=r200_sp,
146                   circle_args={'color':'red',
147                               'linestyle':'dashed'})
148 slc.annotate_sphere(sphere_center,
149                   radius=r500_sp,
150                   circle_args={'color':'black',
151                               'linestyle':'dashed'})
152 slc.set_zlim(("gas","temperature"), 1.0e2, 1.0e8)
153 slc.show()
154 # %%
155 # Off-axis projection (if needed)
156 prj = yt.OffAxisProjectionPlot(ds,
157                                [1,1,1],
158                                ("gas","density"),

```



```

159         width=(10, "Mpc"),
160         center=c)
161 prj.set_zlim(("gas","density"), 1.0e-5, 1.0)
162 prj.show()
163 # %%
164 # Hot gas density
165 sphere_center = c
166 r0_pt = ds.quan(10, 'kpc')
167 r200_sp = ds.quan(696.5179446533203 , 'kpc')
168 r500_sp = ds.quan(436.4346303222656 , 'kpc')
169 prj = yt.ProjectionPlot(ds,
170                          "x",
171                          ("hot_gas","density"),
172                          width=(2, "Mpc"),
173                          center=c_shifted)
174 prj.annotate_sphere(c_shifted,
175                    radius=r0_pt,
176                    circle_args={'color':'black',
177                                 'linestyle':'solid'})
178 prj.annotate_sphere(sphere_center,
179                    radius=r200_sp,
180                    circle_args={'color':'red',
181                                 'linestyle':'dashed'})
182 prj.annotate_sphere(sphere_center,
183                    radius=r500_sp,
184                    circle_args={'color':'black',
185                                 ↪ 'linestyle':'dashed'})
186 prj.set_zlim(("hot_gas","density"), 1.0e-7, 1.0e-2)
187 prj.show()
188 # %%
189 # Eventually save the projection and slice plots
190 prj.save(f"prj_h{haloID}.pdf")
191 slc.save(f"slc_h{haloID}.pdf")
192 # %%
193 # ----- Getting region info and physical quantities -----
194 width = ds.quan(0.15, "Mpc")
195 le = c_shifted - 0.5*width
196 re = c_shifted + 0.5*width
197 box = ds.box(le, re)
198

```

## C. CODE: LOADING AND HANDLING OF TNG DATA STRUCTURE

```
199 # This is the way to obtain quantities from a small box within
    ↪ the coordinates of "box", along with some terrible factors
    ↪ to translate from TNG simulation comoving units to the
    ↪ units ordinary astrophysicists (such as we are) often use.
200
201 abundance = np.average(box[('hot_gas', 'metallicity')])/0.0127
202 abundance_err = np.std(box[('hot_gas', 'metallicity')])/0.0127
203 print("Z :: Abundance :", abundance.value, "pm",
    ↪ abundance_err.value, "Z_solar")
204 # %%
205 temperature = np.average(box[('hot_gas', 'temperature')],
    ↪ weights=box[('hot_gas', 'density')])
206 average = np.average(box[('hot_gas', 'temperature')],
    ↪ weights=box[('hot_gas', 'density')])
207 variance = np.average((box[('hot_gas',
    ↪ 'temperature')]-average)**2, weights=box[('hot_gas',
    ↪ 'density')])
208 weighted_std = np.sqrt(variance)*8.617333262145e-8
209 tempkev = temperature*8.617333262145e-8
210 print("Temperature in keV :", tempkev.value, "pm",
    ↪ weighted_std.value, "keV")
211 # %%
212 density = np.average(box[('PartType0', 'Density')])
    ↪ *((2e+40)/1.67e-27)/(((3.09e+19)**3)*(0.6774**2)*100**3)
213 density_err = np.std(box[('PartType0', 'Density')])
    ↪ *((2e+40)/1.67e-27)/(((3.09e+19)**3)*(0.6774**2)*100**3)
214 print("mean density :", density.value, "pm", density_err.value,
    ↪ "particles/cm3")
215 # halo_mass = groupcat['Group_M_Crit200'][haloID]*0.6774*1e10
216 # print("halo_mass :", halo_mass, "M_solar")
217 r200 = halo["Group_R_Crit200"]*0.6774
218 print("r200 :", r200, "kpc")
219 r500 = halo["Group_R_Crit500"]*0.6774
220 print("r500 :", r500, "kpc")
221 # %%
```

## D Code: mock observations and spectra acquisition

The following Appendix D is a code used for simulating mock observations and spectra along with saving all the files created in the process: photon lists, event simput catalogs, images or spectra itself.

```
1  # %%
2  # ----- Mock observation - configuration -----
3  emin = 0.2
4  emax = 12.0
5  nbins = 4000
6  source_model = pyxsim.CIESourceModel(
7      "apec", emin, emax, nbins, ("hot_gas","metallicity"),
8      temperature_field=("hot_gas","temperature"),
9      emission_measure_field=("hot_gas", "emission_measure"),
10 )
11 # %%
12 exp_time = (100, "ks") # exposure time
13 area = (3000.0, "cm**2") # collecting area
14 # Note that this collecting area should be bigger than the
15   ↪ collecting area of any of the used telescopes.
16 redshift = 0.01
17 # %%
18 # Create a box from which photons are drawn
19 width = ds.quan(0.15, "Mpc")
20 le = c_shifted - 0.5*width
21 re = c_shifted + 0.5*width
22 box = ds.box(le, re)
23 # %%
24 # ----- Create and project photons -----
25 n_photons, n_cells =
26   ↪ pyxsim.make_photons(f"halo_{haloID}_photons",
27                       box,
28                       redshift,
29                       area,
30                       exp_time,
31                       source_model)
32 # %%
33 n_events = pyxsim.project_photons(f"halo_{haloID}_photons",
34                                  f"halo_{haloID}_events",
35                                  "x",
36                                  (45., 30.),
37                                  absorb_model="wabs",
```

## D. CODE: MOCK OBSERVATIONS AND SPECTRA ACQUISITION

---

```
36                                     nH=0.01)
37 # %%
38 # Additional rotation, if necessary
39 original_axis = np.array([1, 0, 0])
40 rotation_angle_x = 30
41 rotation_angle_y = 20
42 rotation_angle_z = 0
43
44 r_x = R.from_rotvec(np.radians(rotation_angle_x) * np.array([1,
45   ↪ 0, 0]))
46 r_y = R.from_rotvec(np.radians(rotation_angle_y) * np.array([0,
47   ↪ 1, 0]))
48 r_z = R.from_rotvec(np.radians(rotation_angle_z) * np.array([0,
49   ↪ 0, 1]))
50
51 rotated_axis = r_y.apply(r_x.apply(original_axis))
52 # Rotated event file:
53 n_events = pyxsim.project_photons(f"halo_{haloID}_photons",
54   ↪ f"halo_{haloID}_events",
55   ↪ rotated_axis,
56   ↪ (45.,30.),
57   ↪ absorb_model="wabs",
58   ↪ nH=0.01)
59 # %%
60 # Write all to a simput catalog
61 events = pyxsim.EventList(f"halo_{haloID}_events.h5")
62 events.write_to_simput(f"halo_{haloID}", overwrite=True)
63 # %%
64 # ----- Create mock image with SOXS -----
65 exposure = (100.0, "ks") # exposure time of the observation
66
67 # Our instrument menu:
68 # instrument = "chandra_aciss_cy22" # the Chandra we use
69 # instrument = "xrism_resolve" # the XRISM we use
70 # instrument = "NewAthena" # the Athena we use
71 # instrument = "hubs" # the HUBS we use
72 instrument = "lem_inner_array" # the LEM we use
73
74 # %%
75 # ----- Prepare image and spectrum -----
```

```

73 soxs.instrument_simulator(f"halo_{haloID}_simput.fits",
    ↪ f"evts_{instrument}_expks:{exposure[0]}.fits", exposure,
    ↪ instrument, (45,30.), overwrite=True, foreground=True,
    ↪ ptsrc_bkgnd=True, instr_bkgnd=False)
74 # %%
75 # Image
76 soxs.write_image("image.fits",
77                 "image.fits",
78                 emin=0.1,
79                 emax=12.0,
80                 overwrite=True)
81 # %%
82 center_sky = SkyCoord(45, 30, unit='deg', frame='fk5')
83 region_sky = RectangleSkyRegion(center=center_sky,
84                                 width=32*u.arcmin,
85                                 height=32*u.arcmin)
86 with fits.open(f"img_{instrument}_expks:{exposure[0]}.fits") as f:
87     w = wcs.WCS(header=f[0].header)
88     fig, ax = soxs.plot_image("name.fits",
89                               stretch='log',
90                               cmap='afmhot',
91                               vmax=1500.0,
92                               width=0.2)
93 ax.add_artist(region_sky.to_pixel(w).as_artist())
94 # %%
95 # Spectrum
96 soxs.write_spectrum("name.fits",
97                   "spectrum.pi", overwrite=True)
98 fig, ax = soxs.plot_spectrum("spectrum.pi",
99                               xmin=0.3,
100                              xmax=10.0,
101                              xscale="log",
102                              yscale="log")
103 # %%

```

Some filenames and sections were slightly modified within shown code to better fit the thesis setup. All technical parameters however remain functional. For the full code, we again refer the reader to our public GitHub repository at [github.com/madmad02/Bc-Thesis\\_XRS\\_public](https://github.com/madmad02/Bc-Thesis_XRS_public).